

Search for intermediate-mass black hole binaries in the third observing run of Advanced LIGO and Advanced Virgo

- R. Abbott¹, T. D. Abbott², F. Acernese^{3,4}, K. Ackley⁵, C. Adams⁶, N. Adhikari⁷, R. X. Adhikari¹, V. B. Adya⁸, C. Affeldt^{9,10}, D. Agarwal¹¹, M. Agathos^{12,13}, K. Agatsuma¹⁴, N. Aggarwal¹⁵, O. D. Aguiar¹⁶, L. Aiello¹⁷, A. Ain¹⁸, P. Ajith¹⁹, T. Akutsu^{20,21}, S. Albanesi²², A. Allocca^{23,4}, P. A. Altin⁸, A. Amato²⁴, C. Anand⁵, S. Anand¹, A. Ananyeva¹, S. B. Anderson¹, W. G. Anderson⁷, M. Ando^{25,26}, T. Andrade²⁷, N. Andres²⁸, T. Andrić²⁹, S. V. Angelova²⁹, S. Ansoldi^{30,31}, J. M. Antelis³², S. Antier³³, S. Appert¹, K. Arai¹, K. Arai³⁴, Y. Arai³⁴, S. Araki³⁵, A. Araya³⁶, M. C. Araya¹, J. S. Areeda³⁷, M. Arène³³, N. Aritomi²⁵, N. Arnaud^{38,39}, S. M. Aronson², K. G. Arun⁴⁰, H. Asada⁴¹, Y. Asai⁴², G. Ashton⁵, Y. Aso^{43,44}, M. Assiduo^{45,46}, S. M. Aston⁶, P. Astone⁴⁷, F. Aubin²⁸, C. Austin², S. Babak³³, F. Badaracco⁴⁸, M. K. M. Bader⁴⁹, C. Badger⁵⁰, S. Bae⁵¹, Y. Bae⁵², A. M. Baer⁵³, S. Bagnasco²², Y. Bai¹, L. Baiotti⁵⁴, J. Baird³³, R. Bajpai⁵⁵, M. Ball⁵⁶, G. Ballardin³⁹, S. W. Ballmer⁵⁷, A. Balsamo⁵³, G. Baltus⁵⁸, S. Banagiri⁵⁹, D. Bankar¹¹, J. C. Barayoga¹, C. Barbieri^{60,61,62}, B. C. Barish¹, D. Barker⁶³, P. Barneo²⁷, F. Barone^{64,4}, B. Barr⁶⁵, L. Barsotti⁶⁶, M. Barsuglia³³, D. Barta⁶⁷, J. Bartlett⁶³, M. A. Barton^{65,20}, I. Bartos⁶⁸, R. Bassiri⁶⁹, A. Basti^{70,18}, M. Bawaj^{71,72}, J. C. Bayley⁶⁵, A. C. Baylor⁷, M. Bazzan^{73,74}, B. Bécsy⁷⁵, V. M. Bedakihale⁷⁶, M. Bejger⁷⁷, I. Belahcene³⁸, V. Benedetto⁷⁸, D. Beniwal⁷⁹, T. F. Bennett⁸⁰, J. D. Bentley¹⁴, M. BenYalla²⁹, F. Bergamin^{9,10}, B. K. Berger⁶⁹, S. Bernuzzi¹³, C. P. L. Berry^{15,65}, D. Bersanetti⁸¹, A. Bertolini⁴⁹, J. Betzwieser⁶, D. Beveridge⁸², R. Bhandare⁸³, U. Bhardwaj^{84,49}, D. Bhattacharjee⁸⁵, S. Bhaumik⁶⁸, I. A. Bilenko⁸⁶, G. Billingsley¹, S. Bini^{87,88}, R. Birney⁸⁹, O. Birnholtz⁹⁰, S. Biscans^{1,66}, M. Bischi^{45,46}, S. Biscoveanu⁶⁶, A. Bisht^{9,10}, B. Biswas¹¹, M. Bitossi^{39,18}, M.-A. Bizouard⁹¹, J. K. Blackburn¹, C. D. Blair^{82,6}, D. G. Blair⁸², R. M. Blair⁶³, F. Bobba^{92,93}, N. Bode^{9,10}, M. Boer⁹¹, G. Bogaert⁹¹, M. Boldrini^{94,47}, L. D. Bonavena⁷³, F. Bondu⁹⁵, E. Bonilla⁶⁹, R. Bonnand²⁸, P. Booker^{9,10}, B. A. Boom⁴⁹, R. Bork¹, V. Boschi¹⁸, N. Bose⁹⁶, S. Bose¹¹, V. Bossilkov⁸², V. Boudart⁵⁸, Y. Bouffanais^{73,74}, A. Bozzi³⁹, C. Bradaschia¹⁸, P. R. Brady⁷, A. Bramley⁶, A. Branch⁶, M. Branchesi^{29,97}, J. E. Brau⁵⁶, M. Breschi¹³, T. Briant⁹⁸, J. H. Briggs⁶⁵, A. Brillet⁹¹, M. Brinkmann^{9,10}, P. Brockill⁷, A. F. Brooks¹, J. Brooks³⁹, D. D. Brown⁷⁹, S. Brunett¹, G. Bruno⁴⁸, R. Bruntz⁵³, J. Bryant¹⁴, T. Bulik⁹⁹, H. J. Bulten⁴⁹, A. Buonanno^{100,101}, R. Buscicchio¹⁴, D. Buskulic²⁸, C. Buy¹⁰², R. L. Byer⁶⁹, L. Cadonati¹⁰³, G. Cagnoli²⁴, C. Cahillane⁶³, J. Calderón Bustillo^{104,105}, J. D. Callaghan⁶⁵, T. A. Callister^{106,107}, E. Calloni^{23,4}, J. Cameron⁸², J. B. Camp¹⁰⁸, M. Canepa^{109,81}, S. Canevarolo¹¹⁰, M. Cannavacciuolo⁹², K. C. Cannon¹¹¹, H. Cao⁷⁹, Z. Cao¹¹², E. Capocasa²⁰, E. Capote⁵⁷, G. Carapella^{92,93}, F. Carbognani³⁹, J. B. Carlin¹¹³, M. F. Carney¹⁵, M. Carpinteri^{114,115,39}, G. Carrillo⁵⁶, G. Carullo^{70,18}, T. L. Carver¹⁷, J. Casanueva Diaz³⁹, C. Casentini^{116,117}, G. Castaldi¹¹⁸, S. Caudill^{49,110}, M. Cavaglià⁸⁵, F. Cavalier³⁸, R. Cavalieri³⁹, M. Ceasar¹¹⁹, G. Cella¹⁸, P. Cerdá-Durán¹²⁰, E. Cesarini¹¹⁷, W. Chaibi⁹¹, K. Chakravarti¹¹, S. Chalathadka Subrahmanya¹²¹, E. Champion¹²², C.-H. Chan¹²³, C. Chan¹¹¹, C. L. Chan¹⁰⁵, K. Chan¹⁰⁵, M. Chan¹²⁴, K. Chandra⁹⁶, P. Chanial³⁹, S. Chao¹²³, P. Charlton¹²⁵, E. A. Chase¹⁵, E. Chassande-Mottin³³, C. Chatterjee⁸², D. Chatterjee¹¹, D. Chatterjee⁷, M. Chaturvedi⁸³, S. Chaty³³, K. Chatzioannou¹, C. Chen^{126,127}, H. Y. Chen⁶⁶, J. Chen¹²³, K. Chen¹²⁸, X. Chen⁸², Y.-B. Chen¹²⁹, Y.-R. Chen¹³⁰, Z. Chen¹⁷, H. Cheng⁶⁸, C. K. Cheong¹⁰⁵, H. Y. Cheung¹⁰⁵, H. Y. Chia⁶⁸, F. Chiadini^{131,93}, C.-Y. Chiang¹³², G. Chiarini⁷⁴, R. Chierici¹³³, A. Chincarini⁸¹, M. L. Chiofalo^{70,18}, A. Chiummo³⁹, G. Cho¹³⁴, H. S. Cho¹³⁵, R. K. Choudhary⁸², S. Choudhary¹¹, N. Christensen⁹¹, H. Chu¹²⁸, Q. Chu⁸², Y.-K. Chu¹³², S. Chua⁸, K. W. Chung⁵⁰, G. Ciani^{73,74}, P. Ciecielag⁷⁷, M. Cieślar⁷⁷, M. Cifaldi^{116,117}, A. A. Ciobanu⁷⁹, R. Ciolfi^{136,74}, F. Cipriano⁹¹, A. Cirone^{109,81}, F. Clara⁶³, E. N. Clark¹³⁷, J. A. Clark^{1,103}, L. Clarke¹³⁸, P. Clearwater¹³⁹, S. Clesse¹⁴⁰, F. Cleva⁹¹, E. Coccia^{29,97}, E. Codazzo²⁹, P.-F. Cohadon⁹⁸, D. E. Cohen³⁸, L. Cohen², M. Colleoni¹⁴¹, C. G. Collette¹⁴², A. Colombo⁶⁰, M. Colpi^{60,61}, C. M. Compton⁶³, M. Constancio Jr.¹⁶, L. Conti⁷⁴, S. J. Cooper¹⁴, P. Corban⁶, T. R. Corbitt², I. Cordero-Carrión¹⁴³, S. Corezzi^{72,71}, K. R. Corley⁴², N. Cornish⁷⁵, D. Corre³⁸, A. Corsi¹⁴⁴, S. Cortese³⁹, C. A. Costa¹⁶, R. Cotesta¹⁰¹, M. W. Coughlin⁵⁹, J.-P. Coulon⁹¹, S. T. Countryman⁴², B. Cousins¹⁴⁵, P. Couvares¹, D. M. Coward⁸², M. J. Cowart⁶, D. C. Coyne¹, R. Coyne¹⁴⁶, J. D. E. Creighton⁷, T. D. Creighton¹⁴⁷, A. W. Criswell⁵⁹, M. Croquette⁹⁸, S. G. Crowder¹⁴⁸, J. R. Cudell⁵⁸, T. J. Cullen², A. Cumming⁶⁵, R. Cummings⁶⁵, L. Cunningham⁶⁵, E. Cuoco^{39,149,18}, M. Curylo⁹⁹, P. Dababie²⁴, T. Dal Canton³⁸, S. Dall'Osso²⁹, G. Dálya¹⁵⁰, A. Dana⁶⁹, L. M. Daneshgaran Bajastani⁸⁰, B. D'Angelo^{109,81}, S. Daniilishin^{151,49}, S. D'Antonio¹¹⁷, K. Danzmann^{9,10}, C. Darsow-Fromm¹²¹, A. Dasgupta⁷⁶, L. E. H. Datrier⁶⁵, S. Datta¹¹, V. Dattilo³⁹, I. Dave⁸³, M. Davier³⁸, G. S. Davies¹⁵², D. Davis¹, M. C. Davis¹¹⁹, E. J. Daw¹⁵³, R. Dean¹¹⁹, D. DeBra⁶⁹, M. Deenadayalan¹¹, J. Degallaix¹⁵⁴, M. De Laurentis^{23,4}, S. Deléglise⁹⁸, V. Del Favero¹²², F. De Lillo⁴⁸, N. De Lillo⁶⁵, W. Del Pozzo^{70,18}, L. M. De Marchi¹⁵, F. De Matteis^{116,117}, V. D'Emilio¹⁷, N. Demos⁶⁶, T. Dent¹⁰⁴, A. Depasse⁴⁸, R. De Pietri^{155,156}, R. De Rosa^{23,4}, C. De Rossi³⁹, R. De Salvo¹¹⁸, R. De Simone¹³¹, S. Dhurandhar¹¹, M. C. Díaz¹⁴⁷, M. Diaz-Ortiz Jr.⁶⁸, N. A. Didio⁵⁷, T. Dietrich^{101,49}, L. Di Fiore⁴, C. Di Franza¹⁴, C. Di Giorgio^{92,93}, F. Di Giovanni¹²⁰, M. Di Giovanni²⁹, T. Di Girolamo^{23,4}, A. Di Lieto^{70,18}, B. Ding¹⁴², S. Di Pace^{94,47}, I. Di Palma^{94,47}, F. Di Renzo^{70,18}, A. K. Divakarla⁶⁸, A. Dmitriev¹⁴, Z. Doctor⁵⁶, L. D'Onofrio^{23,4}, F. Donovan⁶⁶, K. L. Dooley¹⁷, S. Doravari¹¹, I. Dorrington¹⁷, M. Drago^{94,47}, J. C. Driggers⁶³, Y. Drori¹, J.-G. Ducoin³⁸, P. Dupej⁶⁵, O. Durante^{92,93}, D. D'Urso^{114,115}, P.-A. Duverne³⁸, S. E. Dwyer⁶³, C. Eassa⁶³, P. J. Easter⁵, M. Ebersold¹⁵⁷, T. Eckhardt¹²¹, G. Eddolls⁶⁵, B. Edelman⁵⁶, T. B. Edo¹, O. Edy¹⁵², A. Effler⁶, S. Eguchi¹²⁴, J. Eichholz⁸, S. S. Eikenberry⁶⁸, M. Eisenmann²⁸, R. A. Eisenstein⁶⁶, A. Ejlli¹⁷, E. Engelby³⁷, Y. Enomoto²⁵, L. Errico^{23,4}, R. Essick¹⁵⁸, H. Estellés¹⁴¹, D. Estevez¹⁵⁹, Z. Etienne¹⁶⁰, T. Etzel¹, M. Evans⁶⁶, T. M. Evans⁶, B. E. Ewing¹⁴⁵, V. Fafone^{116,117,29}, H. Fair⁵⁷, S. Fairhurst¹⁷, A. M. Farah¹⁵⁸, S. Farinon⁸¹, B. Farr⁵⁶, W. M. Farr^{106,107}, N. W. Farrow⁵, E. J. Fauchon-Jones¹⁷, G. Favaro⁷³, M. Favata¹⁶¹, M. Fays⁵⁸, M. Fazio¹⁶², J. Feicht¹, M. M. Fejer⁶⁹, E. Fenyesi^{67,163}, D. L. Ferguson¹⁶⁴, A. Fernandez-Galiana⁶⁶, I. Ferrante^{70,18}, T. A. Ferreira¹⁶, F. Fidecaro^{70,18}, P. Figura⁹⁹, I. Fiori³⁹, M. Fishbach¹⁵, R. P. Fisher⁵³, R. Fittipaldi^{165,93},

* Corresponding author: W. Del Pozzo, e-mail: walter.delpozzo@unipi.it

ABSTRACT

Intermediate-mass black holes (IMBHs) span the approximate mass range $100-10^5 M_{\odot}$, between black holes (BHs) that formed by stellar collapse and the supermassive BHs at the centers of galaxies. Mergers of IMBH binaries are the most energetic gravitational-wave sources accessible by the terrestrial detector network. Searches of the first two observing runs of Advanced LIGO and Advanced Virgo did not yield any significant IMBH binary signals. In the third observing run (O3), the increased network sensitivity enabled the detection of GW190521, a signal consistent with a binary merger of mass $\sim 150 M_{\odot}$ providing direct evidence of IMBH formation. Here, we report on a dedicated search of O3 data for further IMBH binary mergers, combining both modeled (matched filter) and model-independent search methods. We find some marginal candidates, but none are sufficiently significant to indicate detection of further IMBH mergers. We quantify the sensitivity of the individual search methods and of the combined search using a suite of IMBH binary signals obtained via numerical relativity, including the effects of spins misaligned with the binary orbital axis, and present the resulting upper limits on astrophysical merger rates. Our most stringent limit is for equal mass and aligned spin BH binary of total mass $200 M_{\odot}$ and effective aligned spin 0.8 at $0.056 \text{ Gpc}^{-3} \text{ yr}^{-1}$ (90% confidence), a factor of 3.5 more constraining than previous LIGO-Virgo limits. We also update the estimated rate of mergers similar to GW190521 to $0.08 \text{ Gpc}^{-3} \text{ yr}^{-1}$.

Key words. gravitational waves – stars: black holes – black hole physics

1. Introduction

Black holes are classified according to their masses: stellar-mass black holes (BHs) are those with mass below $\sim 100 M_{\odot}$, formed by stellar collapse, while supermassive BHs (Ferrarese & Ford 2005) at the centers of galaxies have masses above $10^5 M_{\odot}$. Between stellar-mass and supermassive BHs is the realm of IMBHs and BHs with masses in the $100-10^5 M_{\odot}$ range (van der Marel 2004; Miller & Colbert 2004; Ebisuzaki et al. 2001; Koliopanos 2017; Inayoshi et al. 2020).

Stellar evolution models suggest that BHs with masses up to $\sim 65 M_{\odot}$ are the result of core-collapse in massive stars (Woosley 2017, 2019; Giacobbo et al. 2018; Farmer et al. 2019, 2020; Mapelli et al. 2020). The final fate of the star is determined by the mass of the helium core alone. Stars with helium core masses in the $\sim 32-64 M_{\odot}$ range undergo pulsational pair instability, leaving behind remnant BHs of masses below $\sim 65 M_{\odot}$ (Fowler & Hoyle 1964; Barkat et al. 1967). When the helium core mass is in the $\sim 64-135 M_{\odot}$ range pair-instability drives the supernova explosion and leaves no remnant; while stars with a helium core mass greater than $\sim 135 M_{\odot}$ are expected to directly collapse to intermediate-mass BHs. Thus, pair-instability (PI) prevents the formation of heavier BHs from core-collapse, and suggests a mass gap between $\sim 65-120 M_{\odot}$ in the BH population known as PI supernova (PISN) mass gap (Bond et al. 1984; Woosley et al. 2007; Woosley & Heger 2021). Possible IMBH formation channels also include the direct collapse of massive first-generation, low-metallicity Population III stars (Fryer et al. 2001; Heger et al. 2003; Spera & Mapelli 2017; Madau & Rees 2001; Heger & Woosley 2002), and multiple, hierarchical collisions of stars in dense young star clusters (Miller & Hamilton 2002; O’Leary et al. 2006; Giersz et al. 2015; Mapelli 2016), among others. It is not currently known how supermassive black holes form. The hierarchical merger of IMBH systems in a dense environment is among the putative formation channels for supermassive BHs (King & Dehnen 2005; Volonteri 2010; Mezcua 2017; Koliopanos 2017).

Several IMBH candidates are suggested by electromagnetic observations, but these lack conclusive confirmation (Greene et al. 2020). Observations include direct kinematical measurement of the mass of the central BH in massive star clusters and galaxies (Mezcua 2017; Miller & Hamilton 2002; Atakan Gurkan et al. 2004; Anderson & van der Marel 2010; Baumgardt et al. 2003; Pasham et al. 2015; Vitral & Mamon 2021). Other possible evidence of IMBHs includes extrapolation of scaling relations between the masses of host galaxies and their central supermassive BH to the mass range of globular clusters

(Graham 2012; Graham & Scott 2013; Kormendy & Ho 2013). In addition, observations of characteristic imprints on the surface brightness, mass-to-light ratio and/or line-of-sight velocities also suggest that dense globular clusters harbour IMBHs (van den Bosch et al. 2006; Gebhardt et al. 2005; Noyola et al. 2008; Lützgendorf et al. 2011; Kızıltan et al. 2017). Controversy exists regarding the interpretation of these observations, as some of them can also be explained by a high concentration of stellar-mass BHs or the presence of binaries (Baumgardt et al. 2003; Anderson & van der Marel 2010; Lanzoni et al. 2013). Empirical mass scaling relations of quasi-periodic oscillations in luminous X-ray sources have also provided evidence of IMBHs (Remillard & McClintock 2006). Ultraluminous X-ray sources exceed the Eddington luminosity of an accreting stellar-mass BH (Kaaret et al. 2017; Farrell et al. 2009). An accreting IMBH is a favored explanation in several cases (Kaaret et al. 2001; Miller & Colbert 2004). However, neutron stars or stellar-mass BH emitting above their Eddington luminosity could also account for such observations (Bachetti et al. 2014; Israel et al. 2017). The strongest IMBH candidate among them is HLX-1, an hyper-luminous X-ray source indicating an IMBH mass of $\sim 0.3-30 \times 10^4 M_{\odot}$ (Farrell et al. 2009; Godet et al. 2009; Servillat et al. 2011; Webb et al. 2012; Cseh et al. 2015; Soria et al. 2012). In Lin et al. (2018), an intermediate-mass black hole candidate was found in a tidal disruption event in a massive star cluster. More recently Paynter et al. (2021) claimed an IMBH detection through a gravitationally lensed gamma-ray burst.

The Advanced LIGO (Aasi et al. 2015) and Advanced Virgo (Acernese et al. 2015) interferometric gravitational wave (GW) detectors completed three observing runs between September 2015 and March 2020. The third observing run of Advanced LIGO and Advanced Virgo, O3, extended from April 1, 2019, 15:00 UTC to March 27, 2020 17:00 UTC. The recently released second gravitational-wave transient catalog provided a comprehensive summary of significant compact binary coalescence events observed up to October 1st, 2019 (Abbott et al. 2021a), reporting a total of 50 events. The corresponding binary black hole (BBH) population analysis of Abbott et al. (2021b) indicates that 99% of primary BH masses lie below $m_{99\%} \sim 60 M_{\odot}$; thus, the large majority of merging BHs have masses below a limit of $\sim 65 M_{\odot}$, consistently with expectations from PI.

Near the beginning of O3, an unusually high mass black hole coalescence, GW190521 (Abbott et al. 2020a), was detected. This GW signal was consistent with a coalescence of black holes of $85^{+21}_{-14} M_{\odot}$ and $66^{+17}_{-18} M_{\odot}$ which resulted in a remnant black hole of $142^{+28}_{-16} M_{\odot}$ falling in the mass range of intermediate-mass

black holes¹. GW190521 provided the first conclusive evidence for the formation of an IMBH below $10^3 M_\odot$. It is a massive binary black hole system with an IMBH remnant and a primary BH in the PISN mass gap with high confidence (Abbott et al. 2020b; although, see Fishbach & Holz 2020; Nitz & Capano 2021 for an alternative interpretation). The discovery triggered a variety of investigations regarding the evolution models and the subsequent mass gap in the BH population. It also suggested the possibility of the formation of massive BHs ($>100 M_\odot$) via a hierarchical merger scenario in a dense environment (Abbott et al. 2020b; Kimball et al. 2021).

The Advanced LIGO and Advanced Virgo detectors are sensitive to the lower end of the IMBH binary mass range, potentially making IMBHs detectable out to cosmological distances, as is evident from GW190521. Observation of IMBH binary systems are not only interesting for massive BH formation channels, but they act as a perfect laboratory to test general relativity (Abbott et al. 2016a; Yunes et al. 2016; Yunes & Siemens 2013; Gair et al. 2013). Massive BH coalescences produce louder mergers and ringdown signals in the sensitive band of the advanced GW detectors. Furthermore, these can display prominent higher order modes that confer GWs a more complex morphology that can significantly deviate from a canonical chirp (Calderon Bustillo et al. 2020). Observations of higher order modes help to test general relativity and fundamental properties of BHs such as the no-hair theorem (Kamaretsos et al. 2012; Meidam et al. 2014; Thrane et al. 2017; Carullo et al. 2018) and BH kick measurements (Gonzalez et al. 2007; Campanelli et al. 2007; Calderón Bustillo et al. 2018). These IMBHs might be multiband events observable by both LIGO and Virgo and LISA (Amaro-Seoane et al. 2017), and could provide novel probes of cosmology and contribute to the stochastic background (Fregeau et al. 2006; Miller 2009; Jani et al. 2020; Ezquiaga & Holz 2021).

The GW signal from a massive BBH coalescence is evident as a short-duration waveform with little inspiral and mostly merger-ringdown signal, falling in the low-frequency region of the advanced detectors. With initial GW detectors (Abadie et al. 2012; Aasi et al. 2014), the IMBH binary searches were restricted in order to probe the merger-ringdown phase of the coalescing BBH system using the model waveform-independent coherent WaveBurst (cWB) (Klimenko & Mitselmakher 2004; Klimenko et al. 2005, 2006) and a ringdown templated search (Aasi et al. 2014). Improvement in the detector sensitivity at low frequencies in the advanced era made IMBH binaries a target for a matched filtering search that would probe the short inspiral phase. In Abbott et al. (2017a), we used a combined search with the matched filtering GstLAL (Messick et al. 2017; Hanna et al. 2020; Sachdev et al. 2019) search and model-independent cWB (Klimenko et al. 2011, 2016). This combined search was further extended with an additional matched filtering PyCBC search (Usman et al. 2016; Allen 2005; Dal Canton et al. 2014; Nitz et al. 2017) in Abbott et al. (2019a) using the data from the first two observing runs. No significant IMBH binary event was found in these searches.

While all the previous matched filtering searches were generic BBH searches, the improvements in the detector sensitivity at low frequencies and the IMBH merger signals' short

duration nature motivated us to use matched filter searches targeted to the IMBH mass-spin parameter space. We carried out an IMBH binary search using the entire year-long third observing run, O3, of the Advanced LIGO and Advanced Virgo detector networks with a combined search using three search algorithms: two matched-filtering-based IMBH binary searches using the PyCBC and GstLAL libraries, and the minimally modeled time-frequency-based cWB search. We searched for massive binary systems with at least one component above the expected PISN mass gap limit of $65 M_\odot$, and with an IMBH remnant. GW190521 remains the most significant candidate in the combined search; no other event is comparably significant. We provide the results from the combined search with the next most significant events and follow-up investigations to assess their origins.

The increased sensitivity of the O3 run allows us to set more stringent bounds on the binary merger rate density. The lack of a confirmed IMBH population as well as possible formation channels of IMBH distinct from those of stellar-mass BHs preclude us from using an overall mass model for the IMBH population. Thus, we confined all the upper limit studies to a suite of discrete points in the IMBH parameter space. We incorporated more detailed physics in selecting the suite of IMBH binary waveforms as compared to earlier upper limit studies. In Abbott et al. (2017a), we simulated a limited set of discrete mass and aligned-spin binary waveforms in the first advanced detector observation data to obtain upper limits on the merger rate. The study with the first two observation runs used the most realistic numerical relativity (NR) simulation set with aligned spins for the upper limit study (Abbott et al. 2019a). The most recent stringent merger rate upper limit is $0.2 \text{ Gpc}^{-3} \text{ yr}^{-1}$; this is for the equal mass binary system with a component mass of $100 M_\odot$ and component spins of dimensionless magnitude 0.8 aligned with the binary orbital angular momentum. Recently, Chandra et al. (2020) used IMBH binary systems with generically spinning BHs with total masses from $210\text{--}500 M_\odot$ and obtained a most stringent upper limit of $0.28 \text{ Gpc}^{-3} \text{ yr}^{-1}$ for equal-mass binaries with total mass of $210 M_\odot$.

We used a suite of NR simulations of GW emission from an IMBH binary system with generically spinning BHs in order to estimate our search sensitivity over the O3 data. We placed the most stringent 90% merger rate upper limit on equal mass and aligned spin BH binary of total mass $200 M_\odot$ and with individual BH spins of 0.8 as $0.056 \text{ Gpc}^{-3} \text{ yr}^{-1}$. The revised limit is a factor of ~ 3.5 more stringent than that obtained with the first two observing runs. We also updated the merger rate for systems compatible with the source parameters of GW190521 (first estimated in Abbott et al. 2020b) at $0.08_{-0.07}^{+0.19} \text{ Gpc}^{-3} \text{ yr}^{-1}$ using the combined search method applied to simulated signals injected over the entire O3 data.

The paper is organized as follows: Sect. 2 summarizes the data being used for the search. Section 3 summarizes the combined search approach from the results from three distinct IMBH binary search algorithms. Section 4 discusses the search results and follow-up of the most significant candidate events. Section 5 provides a detailed discussion about the NR GW injection set used and the rate upper limits studied including the updated rate on the most significant GW190521-like systems.

2. Data summary

We carried out the analysis using O3 data from both LIGO detectors (LHO-LIGO Hanford Observatory and LLO-LIGO Livingston Observatory) and the Virgo detector. We conditioned the

¹ The parameter estimated values for GW190521 reported in GWTC-2 are slightly different from that of the detection paper. The estimation in the detection paper is based on the NRSur7dq4 waveform model, and GWTC-2 values are obtained from the estimates averaged over three waveforms; SEOBNRv4PHM, NRSur7dq4, and IMRPhenomPv3HM, respectively.

data in multiple steps before performing our search (Abbott et al. 2020c). The strain data, recorded from each detector, were calibrated in near-real time to produce an online data set (Viets et al. 2018; Acernese et al. 2018). A higher latency offline calibration stage identifies systematic errors and calibration configuration changes (Sun et al. 2020; Estevez et al. 2021). The analyses presented here use the offline recalibrated data from the LIGO detectors, and the Virgo detector’s online data. For this search, we considered 246.2 days, 254.1 days, and 250.8 days of observing-mode data from the Hanford, Livingston, and Virgo detectors, respectively. The joint observation time for the full network of three detectors is 156.4 days.

We then linearly subtracted spectral features of known instrumental origin using auxiliary witness sensors; that is, sensors that indicate the presence of noise causing these features. The subtraction removes calibration lines in all detectors, as well as 60 Hz harmonics produced by power mains coupling in the LIGO detectors (Driggers et al. 2019; Davis et al. 2019). Low-frequency modulation of the power mains coupling also results in side-bands around the 60 Hz line; we applied an additional non-linear noise subtraction to remove these side bands (Vajente et al. 2020).

Periods of poor data quality are marked using data quality flags separated into three categories (Abbott et al. 2020c; Fisher et al. 2020; Davis et al. 2021), which we used to exclude time segments from different searches, as described below. Category 1 flags indicate times when a detector is not operating or recording data in its nominal state; these periods are not analyzed by any search. Category 2 flags indicate periods of excess noise that are highly likely to be caused by known instrumental effects. The cWB and PyCBC searches use different sets of category 2 flags. The GstLAL search does not use category 2 flags, as discussed in Sect. 3. Category 3 flags are based on statistical correlations with auxiliary sensors. Of the analyses presented here, only the cWB search uses category 3 flags.

The candidate events in this paper are vetted in the same way as past GW events (Abbott et al. 2016b, 2021a). This validation procedure identifies data quality issues such as non-stationary noise or glitches of instrumental origin appearing in the strain data. Auxiliary sensors that monitor the detectors and environmental noise are used to check for artifacts that may either have accounted for, or contaminated, the candidate signal (Nguyen et al. 2021). For candidate events that coincide with glitches, subtraction of the glitches from the strain data was performed if possible (Cornish & Littenberg 2015; Littenberg et al. 2016; Pankow et al. 2018); otherwise recommendations are made to exclude the relevant time or frequency ranges from parameter estimation analyses. Validation assessments for individual candidate events are provided in Sect. 4 and Appendix A.

3. Search methods

In this section, we describe the analysis methods’ algorithms (pipelines) used to search the LIGO-Virgo data from O3 for IMBH binary merger signals. Such signals have short durations in the detectors’ sensitive frequency band of typically less than 1 s. Thus, methods for the detection of generic short transient GW events (bursts) may be competitive compared to search methods that use parameterized models of the expected signals (templates) from binary coalescences (e.g. Chandra et al. 2020). As in the IMBH binary search of O1 and O2 (Abbott et al. 2017a, 2019a), we employed both generic transient search meth-

ods and modeled template searches. We first describe the generic transient pipeline, cWB, in the configuration used here, and then the two template based pipelines, GstLAL and PyCBC, which have been adapted to maximize sensitivity to IMBH binary mergers. We then summarize the method used to combine the search outputs into a single candidate list and finally discuss selection criteria to distinguish IMBH binary candidates from the known heavy stellar-mass BBH population (Abbott et al. 2021a,b).

The output of a transient search algorithm or pipeline is a set of candidate events, each with an estimated time of peak strain at the participating detector(s)². Each event is also assigned a ranking statistic value, and its significance is quantified by estimating the corresponding false alarm rate (FAR), which is the expected number of events per time that have an equal or higher ranking statistic value caused by detector noise.

The sensitivity of a search to a population of IMBH mergers can be evaluated by adding simulated signals (injections) to real GW detector strain data and analyzing the resulting data streams to output the ranking statistic and estimated FAR that each simulated signal would be assigned if present in an actual search. Specific simulation campaigns will be described in detail in Sect. 5 and sensitivity estimates from individual search pipelines are included in a public data release.

3.1. cWB model waveform-independent search for IMBH binaries

cWB (Klimenko & Mitselmakher 2004; Klimenko et al. 2005, 2006, 2011, 2016; Drago et al. 2020) is a GW search that uses minimal assumptions on signal morphology to detect and reconstruct GW transients. The search identifies coincident energy across the network of detectors to classify GW signals. The cWB search has been participating in the search for IMBH signals since Initial LIGO’s fifth science run (Abadie et al. 2012). The algorithm uses a multi-resolution wavelet transform, known as the Wilson Daubechies Meyer wavelet transform (Necula et al. 2012), to map the multi-detector data into the time-frequency domain, as blocks of a fixed time-frequency area known as pixels. The algorithm selects pixels with excess energy above the expected noise fluctuation and groups them into clusters, referred to as candidate events. The collection and clustering of pixels differ based on the target source (Klimenko et al. 2016). Each candidate event is ranked according to its coherent signal-to-noise ratio (S/N) statistic (Klimenko et al. 2016), which incorporates the estimated coherent energy and residual noise energy. An additional threshold is applied to the network correlation which provides the measure on the event correlation across multiple detectors in the network. The cWB algorithm reconstructs the source sky location and whitened signal waveforms using the constrained maximum likelihood method (Klimenko et al. 2016).

We estimated the FAR of a search event with time lag analysis: data from one or more detectors were time-shifted by more than 1 s with respect to other detectors in the network; then, cWB identifies events in this time-shifted data. Since the time shift is greater than the GW time of flight between detectors, this analysis estimates the rate and distribution of false alarms. The analysis is repeated many times with different time-shifts, yielding a total analyzed background time T_{bkg} . For a given search event, the FAR value is estimated as the number of background events

² For black hole binary mergers, this peak strain time is close to the formation of a common horizon.

with coherent S/N greater than the value assigned to the event, divided by T_{bkg} .

The model-independent nature of cWB search makes it susceptible to the incorrect classification of noise artifacts. We applied a series of signal-dependent vetoes based on the time-frequency morphology and energy distribution properties to remove spurious noisy transients. We tuned the veto values based on the extensive simulation of IMBH binary signals (see Appendix A of [Gayathri et al. 2019](#)). We divided the cWB search for quasi-circular BBH signals into two separate configurations: a high-mass search and a low-mass search, depending on the central frequency f_c of the GW signal. For a compact binary merger signal, f_c is inversely proportional to the redshifted total mass $M_z = (1+z)M$, where M is the source frame total mass and z is the source redshift. We then optimized the low-mass search sensitivity for signals with $f_c > 80$ Hz (the BBH regime), and the high-mass search sensitivity for signals with $f_c < 80$ Hz (the IMBH regime). In practice, a cut $f_c > 60$ Hz was imposed in the low-mass search and $f_c < 100$ Hz in the high-mass search, resulting in an overlap region covering 60–100 Hz. In the O3 search, we combined the two searches by applying a trials factor of 2 to the estimated FAR for events in the overlap region. This improved the overall search sensitivity to borderline IMBH events ([Szczeapnyczk et al. 2021](#)).

The cWB search analyzes data from all three detectors in low latency. However, the follow-up offline cWB analysis does not improve detection efficiency with the inclusion of Virgo. This is primarily due to the additional noise in the Virgo detector. Thus, at a given time, the cWB search uses the best available (most sensitive) two-detector network configuration. This ensures that the cWB search does not analyze the same data with multiple detector configurations. In the case where any event showed high significance in the low latency cWB analysis with the three-detector network and low significance in the offline cWB analysis with the best two-detector configuration, we reanalyzed that observing time with both the LLO-LHO-Virgo and LLO-LHO networks and applied a trial factor of 2 to the minimum FAR over the two networks for the final significance.

3.2. Template-based searches for IMBH mergers

For GW signals whose forms are known or can be theoretically predicted, search sensitivity is optimized by the use of matched filter templates that suppress noise realizations inconsistent with the predicted signals. Since the binary parameters are a priori unknown, a discrete set (bank) of templates is used in order to cover signal parameter values within a predetermined range with a specified minimum waveform accuracy ([Sathyaprakash & Dhurandhar 1991](#); [Owen 1996](#)). General binary black hole coalescence signals bear the imprint of component spins misaligned with the orbital axis, causing orbital precession, and potentially also of orbital eccentricity. It is a so far unsolved problem to implement an optimal search over such a complex space of signals.

Instead, the searches presented here restrict the signal model to the dominant mode of GW emission from quasi-circular, non-precessing binaries ([Ajith et al. 2011](#)), that is, with component spins perpendicular to the orbital plane. Both the GstLAL and PyCBC searches use the SEOBNRv4 waveform approximate ([Bohé et al. 2017](#)) as template waveforms, implemented as a reduced-order model ([Pürrer 2016](#)) for computational speed. These templates may still have high matches to signals from precessing or eccentric binaries; however, in general, sensitivity to

such signals will be reduced due to lower matches with template waveforms.

Each detector's strain time series is then correlated with each template to produce a matched filter time series. Single-detector candidates were generated by identifying maxima of the matched filter S/N above a predetermined threshold value. However, during times of known disturbances in detector operation, or during very high amplitude non-Gaussian excursions in the strain data, candidates are either not produced or are discarded, since such high-S/N maxima are very likely to be artifacts. Signal consistency checks such as chi-squared ([Allen 2005](#)) verifications are also calculated, and single-detector candidates may also be discarded for excessive deviation from the expected range of values.

If two or more detectors are operating, their single-detector candidates are compared in order to identify multi-detector candidate events that are consistent in the template parameters, time of arrival, amplitude, and waveform phase over the detector network. The resulting multi-detector events are then ranked via a statistic that depends on the properties of single-detector candidates and their consistency over the network. Finally, the statistical significance of each multi-detector event is obtained by comparing its statistic value to the distribution expected for noise events, resulting in an estimate of its FAR. In the following subsection, we briefly summarize the methods specific to each of the matched filter pipelines.

3.2.1. GstLAL search

The search for IMBH mergers executed by the matched-filter-based GstLAL pipeline ([Messick et al. 2017](#); [Hanna et al. 2020](#); [Sachdev et al. 2019](#); [Cannon et al. 2021](#)) uses a template bank covering a parameter space of binaries with (redshifted) total masses in the $[50, 600] M_\odot$ range. The mass ratios ($q = m_2/m_1$) of the binary systems covered lie between 1 and 1/10, while their spins are either aligned or anti-aligned with the total angular momentum of the system, with the dimensionless spin magnitude being less than 0.98. The analysis starts at a frequency of 10 Hz.

The S/N threshold applied for single-detector triggers is 4 for the Hanford and Livingston detectors and 3.5 for the Virgo detector. The GstLAL search pipeline applies a signal-consistency test based on the template's auto-correlation over time. The search also uses a signal model to describe the prior probability of a binary from a given source population being detected by each template: the signal model used for this search is uniform in the log of the reduced mass of the binary.

The ranking statistic applied to candidate events is an estimate of the relative probability of the event's parameters being caused by a GW signal as compared to noise, that is, the likelihood ratio. In addition to events formed from triggers from multiple detectors, triggers found in a single detector are also included in the search, albeit with a penalty applied to their ranking to account for the higher probability of noise origin.

The GstLAL search does not use data-quality-based vetoes of category 2 and above. Instead, the search uses data quality information known as iDQ ([Essick et al. 2020](#); [Godwin et al. 2020](#)), from auxiliary channels monitoring the detector, to compute a penalty term in the denominator of the ranking statistic. This has been computed for both single-detector and multi-detector triggers found by the search. The non-coincident and noise-like triggers are then used to estimate the background noise probability density, which is sampled to find the estimated

FAR, corresponding to the likelihood ratio for a candidate (Messick et al. 2017; Sachdev et al. 2019).

3.2.2. PyCBC search

The PyCBC-IMBH search used here (Chandra et al. 2021) covers a target space of redshifted total masses between 100 and 600 M_{\odot} , with component masses greater than $40 M_{\odot}$ and mass ratio between 1/1 and 1/10. The components have dimensionless spins projected onto the orbital axis between -0.998 and 0.998. To reduce false alarms arising from short-duration noise transients (Cabero et al. 2019), we discarded any templates with a duration of less than 0.07 s, measured from the fixed starting frequency of 15 Hz.

The analysis preprocesses the data from each detector by windowing out very high amplitude excursions ($>50\sigma$ deviation from Gaussian noise) in the whitened strain time series (Usman et al. 2016). This gating step significantly suppresses the noise background. The S/N threshold for trigger generation was chosen as 4; any triggers in time marked by a category 2 data quality veto were discarded. We also removed LIGO triggers within $(-1, +2.5)$ s of the center of a gating window, since empirically such times contain many lower-amplitude noise transients correlated with the central high amplitude glitch (Chandra et al. 2021).

Signal-consistency χ^2_r and sine-Gaussian discriminant tests were applied to the remaining triggers (Allen 2005; Nitz 2018). The single-detector S/N were corrected for short-term variation in the detector power spectral density (PSD) (Nitz et al. 2019; Mozzon et al. 2020), and a penalty was applied to triggers with a short-term PSD measure over 10 times the expectation from stationary noise (Chandra et al. 2021). The analysis also penalizes triggers with χ^2_r values above 10, where the expectation for a well-matched signal is unity. These vetoes significantly reduce the background.

The search identifies candidates by checking the consistency between triggers in 2 or 3 detectors. The resulting candidates are ranked using the expected distribution of astrophysical signal S/N, phases and times over multiple detectors, as well as models of the non-Gaussian noise distribution in each template and detector (Nitz et al. 2017; Davies et al. 2020). A FAR is assigned to each candidate event by simulating the background noise distribution using time-shifted analyses (Usman et al. 2016), similarly to cWB. The FARs for events involving different detector combinations are finally combined, as in Davies et al. (2020).

Other PyCBC-based searches overlapping the IMBH parameter region were recently presented in Nitz et al. (2019) and Abbott et al. (2021a) using two strategies: a broad parameter space search covering compact binaries with components as neutron stars up to IMBH, and a “focused” search for BBH covering a restricted range of masses and with strict cuts to suppress noise artifacts. The sensitivity of the present IMBH search (at a FAR threshold of 0.01 yr^{-1}) to a set of simulated, generically spinning binary merger signals is increased relatively to the broad (BBH) PyCBC searches of Abbott et al. (2021a) by a factor of ~ 1.5 (~ 1.1) in volume time (VT) for a redshifted total mass of $M_z \in [100-200] M_{\odot}$, and up to a factor ~ 2.8 (~ 12.6) for $M_z \in [450, 600] M_{\odot}$ (Chandra et al. 2021).

3.3. Combined search

Each of our three targeted searches produces a list of candidates characterized by GPS times and FAR values. The p value for

each candidate in a given search, defined as the probability of observing one or more events from the noise alone with a detection statistic as high as that of the candidate, is then

$$p = 1 - e^{-T \cdot \text{FAR}}, \quad (1)$$

where T is the total duration of data analyzed by the search. We combined these lists to form a single list of candidates by first checking whether any events from different searches fall within a 0.1 s time window of each other; if so, we only selected the event with the lowest p value p_{\min} . The resulting clustered events are ranked by a combined p value:

$$\bar{p} \equiv 1 - (1 - p_{\min})^m, \quad (2)$$

where m denotes the trial (look-elsewhere) factor (Abbott et al. 2017a, 2019a). We took $m = 3$ under the assumption that the noise backgrounds of our searches are independent of one another. If there is any correlation between these backgrounds, the effective trial factor will be lower, which makes $m = 3$ a conservative choice.

3.4. Selection of intermediate-mass black hole binaries

As noted in Abbott et al. (2021a,b), LIGO-Virgo observations include a population of black hole binaries with component masses extending up to $60 M_{\odot}$ or above and remnant masses extending up to $\sim 100 M_{\odot}$; thus, there is a priori no clear separation between such heavy BBH systems and the lightest IMBH binaries. We also expect search pipelines tuned for sensitivity to IMBH mergers to be capable of detecting such heavy stellar-mass BBH, since the overlap of their GW signals with those of IMBH binaries may be large. We indeed find that many such BBH systems occurring within O3a are recovered with high significance by our search.

Here, we only selected those events for which, under the assumption that the signals were produced by a quasi-circular binary black hole merger, we have clear evidence that the remnant is an IMBH of mass above $100 M_{\odot}$, and at least the primary black hole has a mass greater than the lower bound of the pair-instability mass gap. For this, which we made a conservative estimate under the standard assumptions of the $^{12}\text{C}(\alpha, \gamma)^{16}\text{O}$ reaction rate, etc. to be $m_1^* = 65 M_{\odot}$ (see e.g., Woosley 2017; Stevenson et al. 2019; Belczynski et al. 2020; Costa et al. 2021; Tanikawa et al. 2021; Vink et al. 2021). Strong evidence that this is the case for the primary component of GW190521 was presented in Abbott et al. (2020a,b). Furthermore, we can say with confidence that the maximum component mass of the black hole binary population seen up to O3a is above $\sim 50 M_{\odot}$, even if GW190521 is excluded from the analysis (see Fig. 2 of Abbott et al. 2021b); thus, we placed a more stringent condition on the primary mass to identify potential outliers of this population.

The selection criteria are evaluated as follows. We begin by defining the hypothesis H according to which the detector output time series $d(t)$ is given by

$$d(t) = n(t) + h(t; \theta), \quad (3)$$

where $n(t)$ is the noise time series, taken as a realization of a zero-mean wide-sense stationary stochastic process, and $h(t; \theta)$ is the gravitational wave-signal model dependent on a set of parameters θ . We estimated the parameters θ by computing their posterior probability distribution $p(\theta|d, H)$ using Bayes’ theorem:

$$p(\theta|d, H) = p(\theta|H) \frac{p(d|\theta, H)}{p(d|H)}, \quad (4)$$

Table 1. Events from the combined search for intermediate-mass black hole binary mergers in O3 data, sorted by their combined p -value \bar{p} .

Events	GPS time	cWB FAR (yr $^{-1}$)	PyCBC FAR (yr $^{-1}$)	GstLAL FAR (yr $^{-1}$)	\bar{p}
GW190521	1242442967.5	2.0×10^{-4}	1.4×10^{-3}	1.9×10^{-3}	4.5×10^{-4}
200114_020818 ^(†)	1263002916.2	5.8×10^{-2}	$8.6 \times 10^{+2}$	$3.6 \times 10^{+4}$	1.2×10^{-1}
200214_224526	1265755544.5	1.3×10^{-1}	—	—	2.5×10^{-1}

Notes. ^(†)200114_020818 was recovered by the cWB search using LHO-LLO data with a FAR of 15.87 yr^{-1} and by a follow-up search using LHO-LLO-Virgo data with a FAR of 0.029 yr^{-1} ; the FAR quoted in the table for cWB is derived from the LHO-LLO-Virgo search with a trial factor of 2.

where $p(\theta|H)$ is the prior probability distribution, $p(d|\theta, H)$ is the likelihood function – taken as the normal distribution in the frequency domain, with the variance given by the power spectral density of the data $d(t)$ thanks to the wide-sense stationarity assumption – and

$$p(d|H) = \int d\theta p(\theta|H)p(d|\theta, H) \quad (5)$$

is the evidence for the hypothesis H .

Each potential candidate is followed up with a coherent Bayesian parameter estimation analysis (Veitch et al. 2015; Lange et al. 2017; Wysocki et al. 2019). In these analyses, we modeled the GW signal as represented by precessing quasi-circular waveforms from three different families: NRSur7dq4 (Varma et al. 2019), SEOBNRv4PHM (Ossokine et al. 2020), and IMRPhenomXPHM (Pratten et al. 2021). All considered models include the effects of higher order multipole moments as well as orbital precession due to misaligned BH spins. Details of the analysis configuration follow previously published ones (Abbott et al. 2021a) and are documented in a separate paper (Abbott et al., in prep.). In particular, we considered uniform priors on the redshifted component masses, the individual spin magnitudes, and the luminosity distance proportional to its square modulus. For the source orientation and spin vectors, we employed isotropic priors.

As a quantitative criterion to select a GW event as an IMBH binary, we considered the support of the joint posterior distributions for the primary mass m_1 and of the remnant mass M_f . For reference values $M^* = 100 M_\odot$ and $m_1^* = 65 M_\odot$, we labeled a candidate as an intermediate-mass black hole binary if

$$\int_{M^*}^{+\infty} \int_{m_1^*}^{+\infty} dm_1 dM_f p(M_f, m_1|d, H) \geq p^*, \quad (6)$$

where p^* is a reference probability threshold, chosen to be $p^* = 0.9$. To perform the integral in Eq. (6), we constructed a Gaussian kernel density estimate to interpolate the posterior $p(M_f, m_1|d, H)$ that we used to perform the integral on a grid. Thus, the main list of candidates presented in the following section does not correspond to the complete set of events recovered by the searches, but only to those relevant to a potential astrophysical IMBH population. However, for comparison with earlier results (Abbott et al. 2021a), we also report a full list of events detected by the combined IMBH search in O3a data, including BBH events that do not fall into the IMBH region (see Sect. 4.2). A catalog of confidently detected heavy BBH systems over the complete O3 run will be provided in a subsequent publication as an update to GWTC-2.

The data for some events may not be consistent with the quasi-circular BBH signal plus Gaussian noise model, either because they contain a signal that deviates significantly from this

standard BBH model, or they are affected by detector noise artifacts that cannot be removed or mitigated. In such cases, the values of $p(M_f|d, H)$ and $p(m_1|d, H)$ extracted from the Bayesian analysis may either be inaccurate or meaningless for events arising from instrumental noise or even from a putative astrophysical source that is not a compact binary merger. Such events will not be excluded from results presented here: they are discussed individually in the following sections.

4. Search results

4.1. Candidate IMBH events

The individual searches are applied on the full O3 data with the analysis time of 0.734 yr, 0.747 yr, and 0.874 yr for the cWB, PyCBC-IMBH, and GstLAL-IMBH searches, respectively. In Table 1, we report events satisfying the criteria for potential IMBH binaries from Sect. 3. This is done in increasing order of combined p value (see Eq. (3)) up to and including the most significant event with unambiguous evidence of instrumental noise origin, 200214_224526. For completeness, we also list marginal triggers found by our combined search in Appendix A.

The top-ranked event is GW190521, and it has a highly significant combined p -value of 4.5×10^{-4} . If this signal is from a quasi-circular merger, then the signal is found to be consistent with the merger of two black holes in a mildly precessing orbit with component masses of $85_{-14}^{+21} M_\odot$ and $66_{-18}^{+17} M_\odot$ and a remnant black hole of $142_{-16}^{+28} M_\odot$. This falls in the mass range of intermediate-mass black holes. A full description of GW190521 and its implications can be found in Abbott et al. (2020a,b).

The second-ranked candidate, 200114_020818, was observed on 14 January 2020 at 02:08:18 UTC and identified by the low-latency cWB search in the LHO-LLO-Virgo detector network configuration, with a FAR of $<0.04 \text{ yr}^{-1}$. The event was publicly reported via GCN minutes after the event was observed (Abbott et al. 2019b). Given the significance of the low-latency alert with the three-detector configuration, we employed both LHO-LLO and LHO-LLO-Virgo networks in cWB to estimate the significance for this event: we find FARs of 15.87 yr^{-1} and 0.029 yr^{-1} for these configurations, respectively. The S/N reconstructed by cWB for each network configuration is 12.3 and 14.5, respectively. As mentioned above in Sect. 3.1, we applied a trial factor of 2 to the most significant result, obtaining a FAR of 0.058 yr^{-1} for the cWB search. The combined p value of this event, 0.12, is marginally significant.

We then examined possible environmental or instrumental causes for the candidate signal. Excess vibration noise could have contributed to the signal in the LIGO Hanford detector, as discussed in Appendix B.1. Furthermore, the morphology of 200114_020818 is consistent with a well-studied class of glitches known as Tomtes (Buikema et al. 2020; Davis et al. 2021). These occur multiple times per hour in LIGO Livingston.

Table 2. Candidate events from this search for IMBH mergers in O3a data, including binary black hole mergers outside the IMBH parameter space, and a comparison with previously obtained GWTC-2 results from the template based search algorithms (Abbott et al. 2021a).

Event	cWB FAR (yr^{-1})	PyCBC			GstLAL		Combined \bar{p}
		GWTC-2 Broad	GWTC-2 BBH FAR (yr^{-1})	IMBH	GWTC-2 Broad FAR (yr^{-1})	IMBH	
GW190408_181802	9.5×10^{-4}	$<2.5 \times 10^{-5}$	$<7.9 \times 10^{-5}$	1.6×10^{-2}	$<1.0 \times 10^{-5}$	$<1.0 \times 10^{-5}$	$<1.0 \times 10^{-4}$
GW190413_052954	—	—	7.2×10^{-2}	5.6×10^{-1}	—	$5.4 \times 10^{+3}$	7.1×10^{-1}
GW190413_134308	—	—	4.4×10^{-2}	1.4×10^{-1}	3.8×10^{-1}	$1.2 \times 10^{+3}$	2.7×10^{-1}
GW190421_213856	3.0×10^{-1}	$1.9 \times 10^{+0}$	6.6×10^{-3}	6.1×10^{-3}	7.7×10^{-4}	$1.8 \times 10^{+0}$	1.4×10^{-2}
GW190503_185404	1.8×10^{-3}	3.7×10^{-2}	$<7.9 \times 10^{-5}$	2.5×10^{-3}	$<1.0 \times 10^{-5}$	1.7×10^{-1}	4.0×10^{-3}
GW190512_180714	8.8×10^{-3}	3.8×10^{-5}	$<5.7 \times 10^{-5}$	$4.0 \times 10^{+1}$	$<1.0 \times 10^{-5}$	$<1.0 \times 10^{-5}$	$<1.0 \times 10^{-4}$
GW190513_205428	—	3.7×10^{-4}	$<5.7 \times 10^{-5}$	5.0×10^{-2}	$<1.0 \times 10^{-5}$	2.1×10^{-1}	1.1×10^{-1}
GW190514_065416	—	—	5.3×10^{-1}	$1.1 \times 10^{+0}$	—	$7.6 \times 10^{+2}$	9.2×10^{-1}
GW190517_055101	8.0×10^{-3}	1.8×10^{-2}	$<5.7 \times 10^{-5}$	8.7×10^{-4}	9.6×10^{-4}	2.7×10^{-2}	1.9×10^{-3}
GW190519_153544	3.1×10^{-4}	$<1.8 \times 10^{-5}$	$<5.7 \times 10^{-5}$	$<1.1 \times 10^{-4}$	$<1.0 \times 10^{-5}$	3.9×10^{-3}	2.5×10^{-4}
GW190521	2.0×10^{-4}	$1.1 \times 10^{+0}$	—	1.4×10^{-3}	1.2×10^{-3}	1.9×10^{-3}	4.5×10^{-4}
GW190521_074359	$<1.0 \times 10^{-4}$	$<1.8 \times 10^{-5}$	$<5.7 \times 10^{-5}$	$<2.3 \times 10^{-5}$	$<1.0 \times 10^{-5}$	$<1.0 \times 10^{-5}$	$<1.0 \times 10^{-4}$
GW190602_175927	1.5×10^{-2}	—	1.5×10^{-2}	1.1×10^{-3}	1.1×10^{-5}	$<1.0 \times 10^{-5}$	$<1.0 \times 10^{-4}$
GW190701_203306	3.2×10^{-1}	—	—	$<1.9 \times 10^{-4}$	1.1×10^{-2}	3.8×10^{-2}	4.3×10^{-4}
GW190706_222641	$<1.0 \times 10^{-3}$	6.7×10^{-5}	4.6×10^{-5}	$<1.1 \times 10^{-4}$	$<1.0 \times 10^{-5}$	2.4×10^{-3}	2.5×10^{-4}
GW190727_060333	8.8×10^{-2}	3.5×10^{-5}	3.7×10^{-5}	$<1.2 \times 10^{-4}$	$<1.0 \times 10^{-5}$	4.5×10^{-4}	2.7×10^{-4}
GW190731_140936	—	—	2.8×10^{-1}	6.4×10^{-1}	2.1×10^{-1}	$2.1 \times 10^{+0}$	7.6×10^{-1}
GW190803_022701	—	—	2.7×10^{-2}	1.7×10^{-1}	3.2×10^{-2}	$3.0 \times 10^{+0}$	3.2×10^{-1}
GW190828_063405	$<9.6 \times 10^{-4}$	$<1.0 \times 10^{-5}$	$<3.3 \times 10^{-5}$	$<7.0 \times 10^{-5}$	$<1.0 \times 10^{-5}$	$<1.0 \times 10^{-5}$	$<1.0 \times 10^{-4}$
GW190915_235702	$<1.0 \times 10^{-4}$	8.6×10^{-4}	$<3.3 \times 10^{-5}$	3.8×10^{-4}	$<1.0 \times 10^{-5}$	4.7×10^{-1}	2.2×10^{-4}
GW190929_012149	—	—	—	3.1×10^{-1}	2.0×10^{-2}	$2.9 \times 10^{+1}$	5.0×10^{-1}

Notes. The cWB search algorithm used here is unchanged over GWTC-2. Candidates are sorted by GPS time, and the FAR is provided for each search algorithm. Template-based methods used in GWTC-2 comprise the PyCBC and GstLAL broad parameter space pipelines and the PyCBC BBH-focused pipeline, while the optimized algorithms applied in this search are labeled “IMBH”. The event names encode the UTC date with the time of the event given after the underscore, except for the individually published event GW190521. The GstLAL FAR values have been capped at $1.0 \times 10^{-5} \text{ yr}^{-1}$ and corresponding \bar{p} values have also been capped. For PyCBC events with FAR estimates limited by finite background statistics, an upper limit is stated. The IMBH combined search p values \bar{p} for each event are calculated from Eq. (6) using p values of the cWB, PyCBC-IMBH and GstLAL-IMBH searches. For details of the search configurations and event parameters, we refer the reader to Abbott et al. (2021a).

However, we are not currently able to exclude a putative, morphologically similar astrophysical signal, as there are no known instrumental auxiliary channels that couple to this glitch type. We undertook detailed model-independent event reconstruction and parameter estimation (PE) studies, which are summarized in Appendix B. Although model-independent methods and algorithms produce mutually consistent reconstructions of the event, our analysis using the available quasi-circular BBH merger waveforms does not support a consistent interpretation of the event as a binary merger signal present across the detector network. We cannot conclusively rule out an astrophysical origin for the event; however, it also appears consistent with an instrumental artifact in LLO, coincidentally with noise fluctuations in LHO and Virgo.

The third-ranked event was observed by the cWB pipeline on 14 February, 2020 at 22:45:26 UTC with a combined S/N of 13.1 in the two Advanced LIGO detectors. The event has a $p_{\text{cWB}} = 0.092$ and thus a $\bar{p} = 0.251$. In addition to its marginal significance, the event has characteristics consistent with an instrumental noise transient. Excess noise due to fast scattered light (Soni et al. 2021) is present in both LLO and LHO data. At Livingston, the excess noise extends up to 70 Hz and lasts many seconds before and after the event. The Hanford scattering noise is weaker in amplitude but still overlaps completely with the duration of the event. Since it is the most significant noise event obtained in the combined search with

the cWB pipeline in its production configuration considering only two-detector events, we used 200214_224526 to establish a threshold of significance for inference of IMBH merger rates (for which see Sect. 5). As 200214_224526 is likely caused by detector noise, any events with lower significance may be assumed to have a high probability of noise origin. For completeness, we discuss some marginal events from the combined search in Appendix A.

4.2. Complete O3a search results including BBH

As noted earlier in Sect. 3, the template-based searches have high sensitivity to the known population of heavy stellar-mass BBH mergers, which may be compared to searches deployed in GWTC-2 (Abbott et al. 2021a). Here, we record the complete list of significant events recovered by the combined IMBH search from O3a data in Table 2, and we supply corresponding search results from GWTC-2 for comparison. Specifically, we show outputs from the PyCBC broad parameter space and focused BBH searches (Nitz et al. 2019) and the GstLAL broad parameter space search (Sachdev et al. 2019).

For GW190521, the PyCBC IMBH search yields a FAR of $1.4 \times 10^{-3} \text{ yr}^{-1}$, as compared to 1.1 yr^{-1} for the broad parameter space analysis of Abbott et al. (2020a, 2021a). This significant change was made in part because the PyCBC IMBH search is optimized for shorter duration signals, and it does not consider

potential signals of total mass significantly below $100 M_\odot$; the mass and spin values of GW190521 are also likely not covered by the templates used in earlier PyCBC searches, which imposed a minimum duration of 0.15 s. A similar change in statistical significance is also observed for GW190602_175927 for the same reasons. However, the IMBH search results assign lower significance to GW190519_153544 and GW190706_222641 as compared to the GWTC-2 results.

The GstLAL pipeline recovers the GW190521 event at a FAR of $1.9 \times 10^{-3} \text{ yr}^{-1}$ across the O3 data. This was reported earlier (Abbott et al. 2020a, 2021a) at a FAR of $1.2 \times 10^{-3} \text{ yr}^{-1}$ over O3a. As described in Sect. 3.2.1, the GstLAL pipeline employed a dedicated search for IMBH binaries with better coverage for the heavier mass binaries than the catalog search. Also, the iDQ-based data quality information used to inform the calculation of the ranking statistics now incorporates multi-detector triggers, going against the only single-detector triggers that were used before. Differences in the significance of the events found by the IMBH specific GstLAL search presented here, compared to what was reported for O3a in Abbott et al. (2021a), can be attributed to the differences in the search settings and the data spanning over all of O3.

5. Astrophysical rates of IMBH binary coalescence

Improved detector sensitivity, updated search methods, and the detection of GW190521 allow us to obtain revised bounds on the merger rate (strictly rate density) of IMBH binaries. Due to a lack of knowledge of specific formation channels for IMBH binaries, even more so than for stellar-mass BH binaries, and the sparse observational evidence of any IMBH population, we did not consider any overall mass model for such a population. Instead, we simulated a suite of IMBH binary waveforms for discrete points in parameter space, including generically spinning component BHs derived from NR simulations. A similar campaign was carried out in Abbott et al. (2019a) using NR waveforms for IMBH binaries with component BH spins aligned with the binary orbital axis and injected into the O1 and O2 data.

5.1. Injection set

We now report on the merger rate of IMBH binary sources based on NR simulations computed by the SXS (Mroué et al. 2013), RIT (Healy et al. 2017), and GeorgiaTech (Jani et al. 2016) codes. These simulations include higher order multipoles, which may make important contributions to the detection of high-mass-and low-mass-ratio ($q \leq 1/4$) binaries (Calderón Bustillo et al. 2016). Based on previous studies that measured the agreement between different NR codes (Abbott et al. 2019a), we include the following harmonic modes in our analysis: $(\ell, m) = \{(2, \pm 1), (2, \pm 2), (3, \pm 2), (3, \pm 3), (4, \pm 2), (4, \pm 3), (4, \pm 4)\}$.

We considered 43 IMBH binary sources with fixed source frame masses and spins, shown in Table 3. These 43 sources include a subset of 16 sources investigated in the O1-O2 IMBH binary search. This updated search includes sources with a total mass of up to $800 M_\odot$, and it expands the range of targeted mass ratio q to between $1/1$ – $1/10$. We also further explored the effects of the component spins on detection efficiency. Of the 43 targeted IMBH sources, four have spins aligned with the orbital axis, with effective total spin (Ajith et al. 2011) $\chi_{\text{eff}} \equiv (\chi_{1,\parallel} + q\chi_{2,\parallel})/(1+q) = 0.8$, where χ_\parallel denotes the BH spin resolved

along the orbital axis, and four have anti-aligned spins with $\chi_{\text{eff}} = -0.8$. A further 11 have precessing spins: $\chi_p \neq 0$, where χ_p is the effective spin-precession parameter of Hannam et al. (2014), Schmidt et al. (2015).

The simulated signals for each targeted source point are uniformly distributed in sky location (θ, ϕ) and inclination angle $\cos(\iota)$. The source redshift z is uniformly distributed in comoving volume, according to the TT+lowP+lensing+ext cosmological parameters given in Table 4 of Planck Collaboration XIII (2016), up to a maximum redshift z_{max} . The signals are added to the O3 strain data, that is, injected with a uniform spacing in time approximately every 100 s over the full observing time, $T_0 = 363.38$ days.

To avoid generating injections that are well outside any possible detection range, z_{max} is independently calculated for each IMBH source point. We consider values of redshift z in increments of 0.05 and calculate a conservative upper bound on the optimal three-detector network S/N, S/N_{net} , for each z . To bound the optimal S/N in a single detector, we assume the source is face-on $\cos(\iota) = 1$, located directly overhead the detector, and we estimate the detector’s PSD using ~ 8 h of typical O3 data. For precessing waveforms, the ι is set at 10 Hz. We determined the maximum redshift by requiring the following: $S/N_{\text{net}}(z_{\text{max}}) \sim 5$. This results in a range of z_{max} across all targeted sources from 0.05 for the $(400 + 400) M_\odot$ anti-aligned spin source to 2.75 for the $(100 + 100) M_\odot$ aligned-spin source, as in Table 3.

When generating the injection parameters, we imposed an additional threshold $S/N_{\text{net}} > 5$ to limit the number of simulations injected into detection pipelines that have a negligibly small probability of detection. For this purpose, the S/N_{net} is reestimated, taking into account the randomly selected source position and orientation. We thus assumed simulated events with $S/N_{\text{net}} < 5$ are missed by the search pipelines; these events are, however, accounted for in the calculation of sensitive volume and merger rates.

As stated in Sect. 3, the searches process the remaining injections with the same configuration as used for results from O3 data. This is necessary to obtain unbiased rate estimates. In the case of cWB, injections were processed with the most sensitive two-detector configuration; thus, for consistency, we only considered events recovered in the corresponding offline two-detector search results.

5.2. Sensitive volume time and merger Rate

Here, we calculate limits on the merger rate for points in the binary component mass and spin parameter space described in Table 3 using the loudest event method (Biswas et al. 2009; Abbott et al. 2016c).

To derive the upper limit on merger rate for a given point in source parameter space, we consider the sensitive volume-time, $\langle VT \rangle_{\text{sen}}$, of our combined search to such sources at a p -value threshold of 0.251, which is determined by 200214_224526, the most significant event due to noise in the combined search results. For mergers with given intrinsic parameters, the expected number of detected signals N is related to the merger rate R and to the sensitive volume time as $\langle N \rangle = R \langle VT \rangle_{\text{sen}}$. For each source point, we estimate $\langle VT \rangle_{\text{sen}}$ as a fraction of the total volume time out to its maximum injection redshift z_{max} by counting injected signals that are detected with a combined p value below the threshold and dividing by the total number of injections generated.

Table 3. Summary of the source frame parameters, sensitive volume time, and merger rate density upper limit at 90% confidence.

$M (M_{\odot})$	q	χ_{eff}	χ_p	SIM ID	z_{max}	$\langle VT \rangle_{\text{sen}} [\text{Gpc}^{-3} \text{yr}^{-1}]$	$R_{90\%} [\text{Gpc}^{-3} \text{yr}^{-1}]$
120	1/2	0.00	0.00	SXS:BBH:0169, RIT:BBH:0117:n140, GT:0446	2.00	12.42	0.19
120	1/4	0.00	0.00	SXS:BBH:0182, RIT:BBH:0119:n140, GT:0454	1.35	5.08	0.45
120	1/5	0.00	0.00	SXS:BBH:0056, RIT:BBH:0120:n140, GT:0906	1.15	3.45	0.67
120	1/7	0.00	0.00	SXS:BBH:0298, RIT:BBH:Q10:n173, GT:0568	0.90	1.85	1.24
120	1/10	0.00	0.00	SXS:BBH:0154, RIT:BBH:0068:n100	0.70	0.91	2.52
150	1/2	0.00	0.00	SXS:BBH:0169, RIT:BBH:0117:n140, GT:0446 ^(†)	1.85	12.84	0.30
200	1	0.00	0.00	SXS:BBH:0180, RIT:BBH:0198:n140, GT:0905	1.85	16.04	0.14
200	1/2	0.00	0.00	SXS:BBH:0169, RIT:BBH:0117:n140, GT:0446	1.60	11.67	0.20
200	1/4	0.00	0.00	SXS:BBH:0182, RIT:BBH:0119:n140, GT:0454	1.15	4.80	0.48
200	1/7	0.00	0.00	SXS:BBH:0298, RIT:BBH:Q10:n173, GT:0568	0.80	1.74	1.32
220	1/10	0.00	0.00	SXS:BBH:0154, RIT:BBH:0068:n100	0.60	0.81	2.86
250	1/4	0.00	0.00	SXS:BBH:0182, RIT:BBH:0119:n140, GT:0454	1.00	3.90	0.59
300	1/2	0.00	0.00	SXS:BBH:0169, RIT:BBH:0117:n140, GT:0446	1.15	7.55	0.31
350	1/6	0.00	0.00	SXS:BBH:0181, RIT:BBH:0121:n140, GT:0604	0.60	1.13	2.03
400	1	0.00	0.00	SXS:BBH:0180, RIT:BBH:0198:n140, GT:0905	1.00	5.65	0.41
400	1/2	0.00	0.00	SXS:BBH:0169, RIT:BBH:0117:n140, GT:0446	0.85	4.06	0.57
400	1/3	0.00	0.00	SXS:BBH:0030, RIT:BBH:0102:n140, GT:0453	0.70	2.55	0.90
400	1/4	0.00	0.00	SXS:BBH:0182, RIT:BBH:0119:n140, GT:0454	0.60	1.70	1.36
400	1/7	0.00	0.00	SXS:BBH:0298, RIT:BBH:Q10:n173, GT:0568	0.45	0.68	3.38
440	1/10	0.00	0.00	RIT:BBH:Q10:n173, GT:0568	0.30	0.31	7.51
500	2/3	0.00	0.00	RIT:BBH:0115:n140, GT:0477	0.70	2.39	0.96
600	1	0.00	0.00	SXS:BBH:0180, RIT:BBH:0198:n140, GT:0905	0.55	1.09	2.12
600	1/2	0.00	0.00	SXS:BBH:0169, RIT:BBH:0117:n140, GT:0446	0.50	0.99	2.32
800	1	0.00	0.00	SXS:BBH:0180, RIT:BBH:0198:n140, GT:0905	0.35	0.20	11.76
200	1	0.80	0.00	SXS:BBH:0230, RIT:BBH:0063:n100	2.75	40.34	0.06
400	1	0.80	0.00	SXS:BBH:0230, RIT:BBH:0063:n100	1.55	20.07	0.11
600	1	0.80	0.00	SXS:BBH:0230, RIT:BBH:0063:n100	0.95	6.46	0.36
800	1	0.80	0.00	SXS:BBH:0230, RIT:BBH:0063:n100	0.65	1.36	1.70
200	1	-0.80	0.00	SXS:BBH:0154, RIT:BBH:0068:n100	1.45	11.40	0.20
400	1	-0.80	0.00	SXS:BBH:0154, RIT:BBH:0068:n100	0.75	2.33	0.99
600	1	-0.80	0.00	SXS:BBH:0154, RIT:BBH:0068:n100	0.40	0.29	7.88
800	1	-0.80	0.00	SXS:BBH:0154, RIT:BBH:0068:n100	0.25	0.06	38.27
200	1	0.51	0.42	GT:0803	2.15	27.72	0.08
200	1/2	0.14	0.42	GT:0872	1.90	15.45	0.15
200	1/4	0.26	0.42	GT:0875	1.55	9.20	0.25
200	1/7	0.32	0.42	GT:0888	1.15	4.30	0.54
400	1	0.51	0.42	GT:0803	1.20	11.79	0.20
400	1/2	0.14	0.42	GT:0872	1.05	6.45	0.36
400	1/4	0.26	0.42	GT:0875	0.90	4.28	0.54
400	1/7	0.32	0.42	GT:0888	0.70	2.12	1.08
600	1	0.51	0.42	GT:0803	0.70	3.02	0.76
600	1/2	0.14	0.42	GT:0872	0.60	1.73	1.33
800	1	0.51	0.42	GT:0803	0.45	0.22	10.28

Notes. For the upper limit, we assumed no detection except for the non-spinning system with total mass $M_T = 150 M_{\odot}$ and $q = 1/2$ marked with (\dagger) , for which we assumed one detection. The source spin parameters are defined at a starting frequency of 16 Hz. The gravitational waveforms are selected based on their availability.

Then, taking a uniform prior on R and using the Poisson probability of zero detected signals as a likelihood, we obtain the 90% credible upper limit $R_{90\%} = 2.3/\langle VT \rangle_{\text{sen}}$. The only significant IMBH binary signal in the combined search results is GW190521. However, there is only one mass-spin (marked with \dagger in Table 3) point that is consistent with both its component mass and spin $\chi_{\text{eff}} - \chi_p$ 90% credible regions. Therefore, for that source point, we conservatively used the Poisson probability of having one IMBH binary detection and thus took $R_{90\%} = 3.9/\langle VT \rangle_{\text{sen}}$.

Injections with component masses $(60 + 60) M_{\odot}$ were performed. However, since this parameter point is within the stellar-mass BBH distribution characterized in Abbott et al. (2021b), to which several heavy BBH systems detected in O3a may contribute, we do not quote an upper rate limit. We do, however, state the search sensitivity for such systems in our data release products.

Table 3 summarizes the sensitive volume-time and upper limit on the merger rate for our chosen set of injections. For simulated non-spinning sources, the sensitive volume-time decreases with an increase in total mass but increases with increasing mass ratio q . There are multiple reasons for these trends. First, for a fixed mass ratio, the duration of a signal within the detector bandwidth decreases with increased total mass, even though its overall intrinsic luminosity increases. This is evident if one compares the sensitive volume time obtained for $(80 + 40) M_{\odot}$, $(100 + 50) M_{\odot}$, and $(133 + 67) M_{\odot}$ systems. Second, the amplitude of a source goes down with a decrease in the mass ratio for a fixed total mass. Hence, the sensitivity drops with a decrease in mass ratio. Last, a decrement in mass ratio also increases the contribution coming from subdominant emission multipoles. This significantly affects the GstLAL and PyCBC searches that filter using dominant multipole templates only.

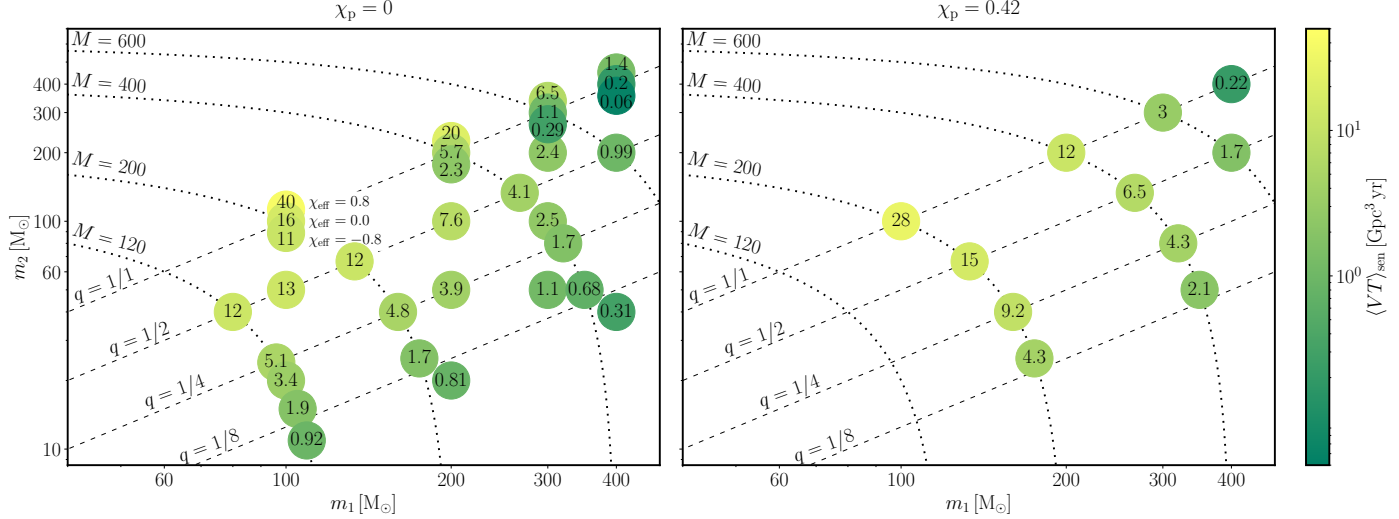


Fig. 1. Averaged sensitive time volume $\langle VT \rangle_{\text{sen}}$ in $\text{Gpc}^{-3} \text{yr}^{-1}$ for the targeted IMBH binary sources in the m_1-m_2 plane. The values are rounded where necessary for visualization. *Left panel:* is for $\chi_p = 0$ and *right panel:* is for $\chi_p = 0.42$. Each circle corresponds to one class of IMBH binaries in the source frame. The χ_{eff} values of injection sets are labeled and shown as displaced circles.

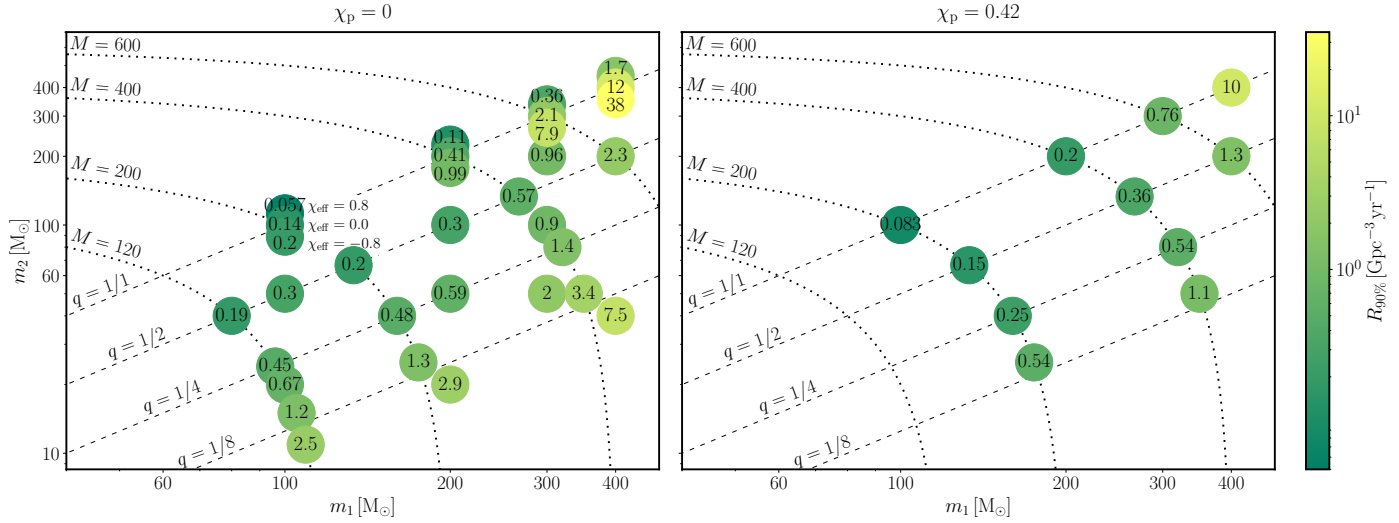


Fig. 2. 90% upper limit on merger rate density $R_{90\%}$ in $\text{Gpc}^{-3} \text{yr}^{-1}$ for the targeted IMBH binary sources in the m_1-m_2 plane. The values are rounded where necessary for display. *Left panel:* $\chi_p = 0$ and *right panel:* for $\chi_p = 0.42$. Each circle corresponds to one class of IMBH binaries in the source frame. The χ_{eff} values of injection sets are labeled and shown as displaced circles.

Concerning the dependence on spins, for more positive (negative) values of the effective inspiral spin of a system, when keeping the source frame component masses fixed, the duration of the merger signal within the detector bandwidth increases (decreases) compared to a non-spinning counterpart. Also, for a binary with fixed mass and fixed non-zero effective precession spin, the total emitted GW energy is higher for aligned spins ($\chi_{\text{eff}} > 0$) compared to anti-aligned spins ($\chi_{\text{eff}} < 0$). Hence, the sensitivity improves (degrades) for systems with positive (negative) effective inspiral spin (Abbott et al. 2019a; Tiwari et al. 2018). All precessing systems used in this analysis have positive χ_{eff} ; hence, the combined search can observe them at a greater distance compared to their non-spinning counterpart. Furthermore, current searches are expected to have a higher sensitive volume for systems with aligned spins, and consequently the merger rate limits for such systems would be lower than in the case of anti-aligned spins.

Figure 1 shows this trend visually. The panels show the sensitive volume time for non-precessing and precessing simulated sources, respectively. Each circle corresponds to one class of IMBH binaries in the source frame. The IMBH binaries with aligned and anti-aligned BH spins, $\chi_{1,2}$, are labeled and shown as displaced circles. In general, we find an increase in the sensitive volume time of the combined search compared to results in Abbott et al. (2019a). This increase is due to an overall increase in the analysis time, detector sensitivity, and the contributing searches' sensitivity.

Figure 2 shows the 90% upper limit on merger rate, $R_{90\%}$, in $\text{Gpc}^{-3} \text{yr}^{-1}$ for the targeted 43 IMBH binary sources in the m_1-m_2 plane. As before, the left panel shows the result for non-precessing simulated sources, whereas the right panel shows the same for precessing simulated sources. We set our most stringent upper limit $0.06 \text{ Gpc}^{-3} \text{yr}^{-1}$ for equal-mass IMBH binaries with total mass $200 M_\odot$ and spin $\chi_{1,2} = 0.8$, which is ~ 3.5 times more stringent than in the previous study (Abbott et al. 2019a).

5.3. Updated GW190521 merger rate estimate

We reestimated the merger rate of a GW190521-like population. As in Abbott et al. (2016c, 2017b, 2020a,b), we considered a simulated signal to be detected if it is recovered with a FAR of less than 100 yr^{-1} . This corresponds to a combined p -value threshold of 0.009. We considered the maximum observed time ($T_a = 0.874 \text{ yr}$) across the three pipelines as the analysis time of the combined search. The population is generated by drawing the intrinsic parameters from the posterior distribution inferred using the NRSur7dq4 waveform model (Abbott et al. 2020b) and then distributing them isotropically over binary orientation parameters and the sky position, and uniformly over comoving volume time up to a max redshift $z = 1.5$.

The sensitive volume time of the combined search to GW190521-like mergers over the entire O3 data is $14.35 \text{ Gpc}^{-3} \text{ yr}^{-1}$. As in Abbott et al. (2020b), we took a Jeffreys prior proportional to $R^{-1/2}$, where R is the astrophysical merger rate. Given the count of one detection above the threshold, we obtain an estimate of $0.08_{-0.07}^{+0.19} \text{ Gpc}^{-3} \text{ yr}^{-1}$, which is more constraining than the estimate given in Abbott et al. (2020b) and consistent with the higher observing time and increased sensitivity of the searches.

6. Discussion and conclusions

The Advanced LIGO and Advanced Virgo detector network concluded their year-long third observing run in March 2020. The first part of the run witnessed a massive black hole merger event (GW190521; Abbott et al. 2020a) with a remnant firmly falling in the IMBH parameter space; the mass was $142_{-16}^{+28} M_\odot$ and the components were $85_{-14}^{+21} M_\odot$ and $66_{-18}^{+17} M_\odot$, thus a primary BH was inferred to be in the PISN mass gap. In this work, we present the IMBH binary search carried out on the entire range of data of the third observing run. We used three GW search algorithms for this search; the two template-based searches Gst-LAL and PyCBC, and one model waveform-independent cWB search. The template-based matched filter searches use the dedicated template bank designed for the massive black hole binary coalescences, while the model waveform independent cWB uses a single detection approach for the entire range of BBHs masses including IMBH binaries. We ranked the events based on the combined significance computed combining the three searches. The search shows that GW190521 is still the most significant IMBH binary event. Besides that, we do not find any other significant event in the combined search. We update the significance of already published O3a events with this combined search. We report the discussion on the candidate events, including the marginal events.

Amongst the remaining events, 200114_020818 shows marginal significance in the offline cWB search. As the detector characterization study does not conclusively demonstrate the origin of this event to be terrestrial, we carried out a follow-up investigation on this event in Appendix B. This includes event reconstruction and residual analysis. While the premerger dynamics of 200114_020818 are barely accessible, we analysed 200114_020818 under the quasi-circular BBH hypothesis. Unlike the case of GW190521, here we find strongly inconsistent results across different waveform approximants. However, the model-independent event reconstructions are consistent with each other. Hence, either the event is not consistent with the available quasi-circular binary black hole waveforms or its origin is non-astrophysical in nature.

We update the merger rate density on a suite of simulated signals for IMBH binary systems with generic BH spins using the numerical relativity waveforms provided by SXS, RIT, and GeorgiaTech catalogs. With the year-long O3 data and improved sensitivity of the combined search, we computed merger rate limits using the method of the loudest confirmed noise trigger. The most stringent merger rate, a 90% upper limit, is placed on equal-mass IMBH binaries with a total mass of $200 M_\odot$ and spin $\chi_{1,2} = 0.8$, as $0.056 \text{ Gpc}^{-3} \text{ yr}^{-1}$. This is a factor ~ 3.5 below the previous limit using O1-O2 data. We further revise the astrophysical merger rate estimate for binary systems comparable to GW190521 to $0.08_{-0.07}^{+0.19} \text{ Gpc}^{-3} \text{ yr}^{-1}$, a factor 1.6 more stringent than the earlier result in Abbott et al. (2020b). A semi-analytical estimate of IMBH merger rate density in globular cluster environments under certain assumptions was performed in Rasskazov et al. (2020) and Fragione et al. (2018). In this study, the calculation of the expected S/N considered quadrupolar GW emission at Newtonian order from quasi-circular, non-spinning binaries; however, the inclusion of the merger and ringdown phases of the signal is expected to have a significant impact on the predicted detection rate. The observational rate upper limits obtained here can provide input into such semi-analytical approaches.

We emphasize that the IMBH binaries pose an extreme challenge to interpret. All current GW observations have so far been interpreted within the canonical scenario of an inspiraling quasi-circular BBH. While this is a safe assumption when the (premerger) inspiral process is clearly visible in the band, the low frequency of IMBH binary signals makes such a putative inspiral barely visible. This leaves the pre-merger dynamics and even the very nature of the colliding objects open to further interpretation, in turn making some conclusions obtained through canonical analyses less robust (Bustillo et al. 2021a). For instance, alternative scenarios have been proposed that GW190521 is consistent with an eccentric binary merger (Romero-Shaw et al. 2020; Gayathri et al. 2022). Moreover, Bustillo et al. (2021b) showed that GW190521 is consistent with the merger of exotic objects that have dramatically different astrophysical conclusions. The primordial BH scenario is explored in De Luca et al. (2021) and Clesse & Garcia-Bellido (2020). An alternative scenario for forming BHs in the mass gap includes gas accretion onto stellar mass BHs in dense molecular clouds or in primordial dense clusters (Roupa & Kazanas 2019; Safarzadeh & Haiman 2020; Rice & Zhang 2021).

With continuous improvement in the sensitivity of advanced detectors, especially in the low-frequency region, we expect to observe higher numbers of inspiral cycles from massive BBH mergers, and hence better probe inspiral dynamics, including the effects of orbital eccentricity and precession on the signal. In addition, systems with asymmetric component masses may be observed, enabling us to probe higher order multipole emissions. Such gravitational-wave signals including higher order multipoles and precession have a complex morphology: future developments in template-based searches to incorporate such complex dynamics (Harry et al. 2018) can be expected to improve the detectability of IMBH binaries with matched-filter based methods. Similarly to the current interferometer network, we expect future detector noise to include a variety of artifacts, including transients (glitches) at a low frequency that may mimic some aspects of IMBH binary signals. Improved veto methods to distinguish between short-duration noise transients and IMBH signals will thus represent a valuable step toward increasing the detection rate, and they may benefit from novel machine-learning-based classification approaches (Jadhav et al. 2021).

The detection of massive BHs in the GW window has provided crucial observational input for the stellar evolutionary models. While we used the conservative limit of the lower edge of the mass gap in the BH population, it is highly uncertain; it might be as low as $\sim 40 M_{\odot}$ or above $\sim 70 M_{\odot}$, depending on uncertainties surrounding the nuclear reaction rates (e.g., Farmer et al. 2019, 2020; Costa et al. 2021), the collapse of the residual stellar envelope (e.g., Mapelli et al. 2020; Costa et al. 2021), the impact of stellar rotation (e.g., Mapelli et al. 2020; Marchant & Moriya 2020; Woosley & Heger 2021), the result of stellar mergers (e.g., Di Carlo et al. 2019, 2020a; Renzo et al. 2020a), the efficiency of accretion from companion stars (e.g., van Son et al. 2020), the model of convection (e.g., Renzo et al. 2020b; Farrell et al. 2021; Tanikawa et al. 2021), and the onset of dredge-up episodes (e.g., Costa et al. 2021; Tanikawa et al. 2021; Umeda et al. 2020). Recently, Costa et al. (2021) proposed that the mass gap might even disappear if a low rate for the $^{12}\text{C}(\alpha, \gamma)^{16}\text{O}$ reaction is assumed and if a mild envelope under-shooting is included in stellar evolution calculations. Theoretical and numerical models show that black holes with mass in the pair instability gap could be the result of hierarchical mergers of smaller black holes (Miller & Hamilton 2002; Antonini & Rasio 2016; Gerosa & Berti 2017; Fishbach et al. 2017; Rodriguez et al. 2019; Kimball et al. 2021; Doctor et al. 2020) or the outcome of stellar collisions in dense star clusters (Di Carlo et al. 2019, 2020b; Kremer et al. 2020; Renzo et al. 2020a). Hierarchical mergers appear to be particularly efficient in nuclear star clusters (Antonini et al. 2019; Fragione et al. 2020; Baibhav et al. 2020; Mapelli et al. 2021) and in the dense gaseous disks of active galactic nuclei (McKernan et al. 2012, 2018; Bartos et al. 2017; Yang et al. 2019; Tagawa et al. 2020, 2021). The detection of more massive BH binaries in the advanced detector era will provide constraints on all the formation channels. In addition, future observations of IMBH binaries across the GW spectrum (Sathyaprakash & Schutz 2009) could strengthen the possible evolutionary link between stellar-mass BHs and supermassive BHs in the galactic centers in coming decades (Mezcua 2017; Koliopanos 2017; King & Dehnen 2005).

Acknowledgements. This material is based upon work supported by NSF's LIGO Laboratory which is a major facility fully funded by the National Science Foundation. The authors also gratefully acknowledge the support of the Science and Technology Facilities Council (STFC) of the United Kingdom, the Max-Planck-Society (MPS), and the State of Niedersachsen/Germany for support of the construction of Advanced LIGO and construction and operation of the GEO600 detector. Additional support for Advanced LIGO was provided by the Australian Research Council. The authors gratefully acknowledge the Italian Istituto Nazionale di Fisica Nucleare (INFN), the French Centre National de la Recherche Scientifique (CNRS) and the Netherlands Organization for Scientific Research, for the construction and operation of the Virgo detector and the creation and support of the EGO consortium. The authors also gratefully acknowledge research support from these agencies as well as by the Council of Scientific and Industrial Research of India, the Department of Science and Technology, India, the Science & Engineering Research Board (SERB), India, the Ministry of Human Resource Development, India, the Spanish Agencia Estatal de Investigación, the Vicepresidència i Conselleria d'Innovació, Recerca i Turisme and the Conselleria d'Educació i Universitat del Govern de les Illes Balears, the Conselleria d'Innovació, Universitats, Ciència i Societat Digital de la Generalitat Valenciana and the CERCA Programme Generalitat de Catalunya, Spain, the National Science Centre of Poland and the Foundation for Polish Science (FNP), the Swiss National Science Foundation (SNSF), the Russian Foundation for Basic Research, the Russian Science Foundation, the European Commission, the European Regional Development Funds (ERDF), the Royal Society, the Scottish Funding Council, the Scottish Universities Physics Alliance, the Hungarian Scientific Research Fund (OTKA), the French Lyon Institute of Origins (LIO), the Belgian Fonds de la Recherche Scientifique (FRS-FNRS), Actions de Recherche Concertées (ARC) and Fonds Wetenschappelijk Onderzoek – Vlaanderen (FWO), Belgium, the Paris Île-de-France Region, the National Research, Development and Innovation Office Hungary (NKFIH), the National Research Foundation of Korea, the Natural Science and Engineering Research Council

Canada, Canadian Foundation for Innovation (CFI), the Brazilian Ministry of Science, Technology, and Innovations, the International Center for Theoretical Physics South American Institute for Fundamental Research (ICTP-SAIFR), the Research Grants Council of Hong Kong, the National Natural Science Foundation of China (NSFC), the Leverhulme Trust, the Research Corporation, the Ministry of Science and Technology (MOST), Taiwan, the United States Department of Energy, and the Kavli Foundation. The authors gratefully acknowledge the support of the NSF, STFC, INFN and CNRS for provision of computational resources. This work was supported by MEXT, JSPS Leading-edge Research Infrastructure Program, JSPS Grant-in-Aid for Specially Promoted Research 26000005, JSPS Grant-in-Aid for Scientific Research on Innovative Areas 2905: JP17H06358, JP17H06361 and JP17H06364, JSPS Core-to-Core Program A. Advanced Research Networks, JSPS Grant-in-Aid for Scientific Research (S) 17H06133, the joint research program of the Institute for Cosmic Ray Research, University of Tokyo, National Research Foundation (NRF) and Computing Infrastructure Project of KISTI-GSDC in Korea, Academia Sinica (AS), AS Grid Center (ASGC) and the Ministry of Science and Technology (MoST) in Taiwan under grants including AS-CDA-105-M06, Advanced Technology Center (ATC) of NAOJ, and Mechanical Engineering Center of KEK. We would like to thank all of the essential workers who put their health at risk during the COVID-19 pandemic, without whom we would not have been able to complete this work.

References

- Aasi, J., et al. (LIGO Scientific Collaboration, Virgo Collaboration) 2014, *Phys. Rev. D*, **89**, 102006
- Aasi, J., et al. (LIGO Scientific Collaboration, Virgo Collaboration) 2015, *Class. Quant. Grav.*, **32**, 074001
- Abadie, J., Abbott, B. P., Abbott, R., et al. 2012, *Phys. Rev. D*, **85**, 102004
- Abbott, B. P., et al. (LIGO Scientific Collaboration, Virgo Collaboration) 2016a, *Phys. Rev. Lett.*, **116**, 221101 [Erratum: Phys. Rev. Lett. 121, 129902 (2018)]
- Abbott, B. P., et al. (LIGO Scientific Collaboration, Virgo Collaboration) 2016b, *Class. Quant. Grav.*, **33**, 134001
- Abbott, B. P., et al. (LIGO Scientific Collaboration, Virgo Collaboration) 2016c, *ApJ*, **832**, L21
- Abbott, B. P., et al. (LIGO Scientific Collaboration, Virgo Collaboration) 2017a, *Phys. Rev. D*, **96**, 022001
- Abbott, B. P., et al. (LIGO Scientific Collaboration, Virgo Collaboration) 2017b, *Phys. Rev. Lett.*, **119**, 161101
- Abbott, B. P., et al. (LIGO Scientific Collaboration, Virgo Collaboration) 2019a, *Phys. Rev. D*, **100**, 064064
- Abbott, R., et al. (LIGO Scientific Collaboration, Virgo Collaboration) 2019b, *GCN*, **25330**, 1
- Abbott, R., et al. (LIGO Scientific Collaboration, Virgo Collaboration) 2020a, *Phys. Rev. Lett.*, **125**, 101102
- Abbott, R., et al. (LIGO Scientific Collaboration, Virgo Collaboration) 2020b, *ApJ*, **900**, L13
- Abbott, B. P., et al. (LIGO Scientific Collaboration, Virgo Collaboration) 2020c, *Class. Quant. Grav.*, **37**, 055002
- Abbott, R., et al. (LIGO Scientific Collaboration, Virgo Collaboration) 2021a, *Phys. Rev. X*, **11**, 021053
- Abbott, R., et al. (LIGO Scientific Collaboration, Virgo Collaboration) 2021b, *ApJ*, **913**, L7
- Acernese, F., Agathos, M., Agatsuma, K., et al. 2015, *Class. Quant. Grav.*, **32**, 024001
- Acernese, F., Adams, T., Agatsuma, K., et al. 2018, *Class. Quant. Grav.*, **35**, 205004
- Ajith, P., Hannam, M., Husa, S., et al. 2011, *Phys. Rev. Lett.*, **106**, 241101
- Allen, B. 2005, *Phys. Rev. D*, **71**, 062001
- Amaro-Seoane, P., Audley, H., Babak, S., et al. 2017, ArXiv e-prints [arXiv:1702.00786]
- Anderson, J., & van der Marel, R. P. 2010, *ApJ*, **710**, 1032
- Antonini, F., & Rasio, F. A. 2016, *ApJ*, **831**, 187
- Antonini, F., Gieles, M., & Gualandris, A. 2019, *MNRAS*, **486**, 5008
- Atakan Gurkan, M., Freitag, M., & Rasio, F. A. 2004, *ApJ*, **604**, 632
- Babak, S., Taracchini, A., & Buonanno, A. 2017, *Phys. Rev. D*, **95**, 024010
- Bachetti, M., Harrison, F. A., Walton, D. J., et al. 2014, *Nature*, **514**, 202
- Baibhav, V., Gerosa, D., Berti, E., et al. 2020, *Phys. Rev. D*, **102**, 043002
- Barkat, Z., Rakavy, G., & Sack, N. 1967, *Phys. Rev. Lett.*, **18**, 379
- Bartos, I., Kocsis, B., Haiman, Z., & M'arka, S. 2017, *ApJ*, **835**, 165
- Baumgardt, H., Hut, P., Makino, J., McMillan, S., & Portegies Zwart, S. F. 2003, *ApJ*, **582**, L21
- Belczynski, K., Hirschi, R., Kaiser, E. A., et al. 2020, *ApJ*, **890**, 113
- Biswas, R., Brady, P. R., Creighton, J. D. E., & Fairhurst, S. 2009, *Class. Quant. Grav.*, **26**, 175009 [Erratum: Class. Quant. Grav. 30, 079502 (2013)]
- Bohé, A., Shao, L., Taracchini, A., et al. 2017, *Phys. Rev. D*, **95**, 044028
- Bond, J. R., Arnett, W. D., & Carr, B. J. 1984, *ApJ*, **280**, 825

- Buikema, A., Cahillane, C., Mansell, G. L., et al. 2020, *Phys. Rev. D*, **102**, 062003
- Bustillo, J. C., Sanchis-Gual, N., Torres-Forné, A., & Font, J. A. 2021a, *Phys. Rev. Lett.*, **126**, 201101
- Bustillo, J. C., Sanchis-Gual, N., Torres-Forné, A., et al. 2021b, *Phys. Rev. Lett.*, **126**, 081101
- Cabero, M., Lundgren, A., Nitz, A. H., et al. 2019, *Class. Quant. Grav.*, **36**, 155010
- Calderón Bustillo, J., Husa, S., Sintes, A. M., & Pürrer, M. 2016, *Phys. Rev. D*, **93**, 084019
- Calderón Bustillo, J., Clark, J. A., Laguna, P., & Shoemaker, D. 2018, *Phys. Rev. Lett.*, **121**, 191102
- Calderon Bustillo, J., Evans, C., Clark, J. A., et al. 2020, *Commun. Phys.*, **3**, 176
- Campanelli, M., Lousto, C. O., Zlochower, Y., & Merritt, D. 2007, *Phys. Rev. Lett.*, **98**, 231102
- Cannon, K., Caudill, S., Chan, C., et al. 2021, *SoftwareX*, **14**, 100680
- Carullo, G., van der Schaaf, L., London, L., et al. 2018, *Phys. Rev. D*, **98**, 104020
- Chandra, K., Gayathri, V., Bustillo, J. C., & Pai, A. 2020, *Phys. Rev. D*, **102**, 044035
- Chandra, K., Villa-Ortega, V., Dent, T., et al. 2021, *Phys. Rev. D*, **104**, 042004
- Clesse, S., & Garcia-Bellido, J. 2020, ArXiv e-prints [arXiv:2007.06481]
- Cornish, N., & Littenberg, T. 2015, *Class. Quant. Grav.*, **32**, 135012
- Cornish, N. J., Littenberg, T. B., Bécsy, B., et al. 2021, *Phys. Rev. D*, **103**, 044006
- Costa, G., Bressan, A., Mapelli, M., et al. 2021, *MNRAS*, **501**, 4514
- Cséh, D., Webb, N. A., Godet, O., et al. 2015, *MNRAS*, **446**, 3268
- Dal Canton, T., Nitz, A. H., Lundgren, A. P., et al. 2014, *Phys. Rev. D*, **90**, 082004
- Dal Canton, T., Nitz, A. H., Gadre, B., et al. 2021, *ApJ*, **923**, 254
- Davies, G. S., Dent, T., Tápai, M., et al. 2020, *Phys. Rev. D*, **102**, 022004
- Davis, D., Massinger, T. J., Lundgren, A. P., et al. 2019, *Class. Quant. Grav.*, **36**, 055011
- Davis, D., Areeda, J. S., Berger, B. K., et al. 2021, *Class. Quant. Grav.*, **38**, 135014
- De Luca, V., Desjacques, V., Franciolini, G., Pani, P., & Riotto, A. 2021, *Phys. Rev. Lett.*, **126**, 051101
- Di Carlo, U. N., Giacobbo, N., Mapelli, M., et al. 2019, *MNRAS*, **487**, 2947
- Di Carlo, U. N., Mapelli, M., Giacobbo, N., et al. 2020a, *MNRAS*, **498**, 495
- Di Carlo, U. N., Mapelli, M., Bouffanais, Y., et al. 2020b, *MNRAS*, **497**, 1043
- Doctor, Z., Wysocki, D., O'Shaughnessy, R., Holz, D. E., & Farr, B. 2020, *ApJ*, **893**, 35
- Drago, M., Gayathri, V., Klimenko, S., et al. 2020, ArXiv e-prints [arXiv:2006.12604]
- Driggers, J. C., Vitale, S., Lundgren, A. P., et al. 2019, *Phys. Rev. D*, **99**, 042001
- Ebisuzaki, T., Makino, J., Tsuru, T. G., et al. 2001, *ApJ*, **562**, L19
- Essick, R., Godwin, P., Hanna, C., Blackburn, L., & Katsavounidis, E. 2020, ArXiv e-prints [arXiv:2005.12761]
- Estevez, D., Lagabbe, P., Masserot, A., et al. 2021, *Class. Quantum Grav.*, **38**, 075007
- Esquiga, J. M., & Holz, D. E. 2021, *ApJ*, **909**, L23
- Farmer, R., Renzo, M., de Mink, S. E., Marchant, P., & Justham, S. 2019, *ApJ*, **887**, 53
- Farmer, R., Renzo, M., de Mink, S. E., Fishbach, M., & Justham, S. 2020, *ApJ*, **902**, L36
- Farrell, S., Webb, N., Barret, D., Godet, O., & Rodrigues, J. 2009, *Nature*, **460**, 73
- Farrell, E., Groh, J. H., Hirschi, R., et al. 2021, *MNRAS*, **502**, L40
- Ferrarese, L., & Ford, H. 2005, *Space Sci. Rev.*, **116**, 523
- Fishbach, M., & Holz, D. E. 2020, *ApJ*, **904**, L26
- Fishbach, M., Holz, D. E., & Farr, B. 2017, *ApJ*, **840**, L24
- Fisher, R. P., Hemming, G., Bizouard, M. A., et al. 2020, ArXiv e-prints [arXiv:2008.11316]
- Fowler, W. A., & Hoyle, F. 1964, *ApJS*, **9**, 201
- Fragione, G., Ginsburg, I., & Kocsis, B. 2018, *ApJ*, **856**, 92
- Fragione, G., Loeb, A., & Rasio, F. A. 2020, *ApJ*, **902**, L26
- Fregeau, J. M., Larson, S. L., Miller, M. C., O'Shaughnessy, R., & Rasio, F. A. 2006, *ApJ*, **646**, L135
- Fryer, C. L., Woosley, S. E., & Heger, A. 2001, *ApJ*, **550**, 372
- Gair, J. R., Vallisneri, M., Larson, S. L., & Baker, J. G. 2013, *Liv. Rev. Relativ.*, **16**, 7
- Gayathri, V., Bacon, P., Pai, A., et al. 2019, *Phys. Rev. D*, **100**, 124022
- Gayathri, V., Healy, J., Lange, J., et al. 2022, *Nat. Astron.*, in press [arXiv:2009.05461]
- Gebhardt, K., Rich, R. M., & Ho, L. C. 2005, *ApJ*, **634**, 1093
- Gerosa, D., & Berti, E. 2017, *Phys. Rev. D*, **95**, 124046
- Ghonge, S., Chatzioannou, K., Clark, J. A., et al. 2020, *Phys. Rev. D*, **102**, 064056
- Giacobbo, N., Mapelli, M., & Spera, M. 2018, *MNRAS*, **474**, 2959
- Giersz, M., Leigh, N., Hypki, A., Lützgendorf, N., & Askar, A. 2015, *MNRAS*, **454**, 3150
- Godet, O., Barret, D., Webb, N. A., Farrell, S. A., & Gehrels, N. 2009, *ApJ*, **705**, L109
- Godwin, P., Essick, R., Hanna, C., et al. 2020, ArXiv e-prints [arXiv:2010.15282]
- Gonzalez, J. A., Sperhake, U., Bruegmann, B., Hannam, M., & Husa, S. 2007, *Phys. Rev. Lett.*, **98**, 091101
- Graham, A. W. 2012, *ApJ*, **746**, 113
- Graham, A. W., & Scott, N. 2013, *ApJ*, **764**, 151
- Greene, J. E., Strader, J., & Ho, L. C. 2020, *ARA&A*, **58**, 257
- Hanna, C., Caudill, S., Messick, C., et al. 2020, *Phys. Rev. D*, **101**, 022003
- Hannam, M., Schmidt, P., Bohé, A., et al. 2014, *Phys. Rev. Lett.*, **113**, 151101
- Harry, I., Bustillo, J. C., & Nitz, A. 2018, *Phys. Rev. D*, **97**, 023004
- Healy, J., Lousto, C. O., Zlochower, Y., & Campanelli, M. 2017, *Class. Quant. Grav.*, **34**, 224001
- Heger, A., & Woosley, S. E. 2002, *ApJ*, **567**, 532
- Heger, A., Fryer, C. L., Woosley, S. E., Langer, N., & Hartmann, D. H. 2003, *ApJ*, **591**, 288
- Inayoshi, K., Visbal, E., & Haiman, Z. 2020, *ARA&A*, **58**, 27
- Israel, G. L., Belfiore, A., Stella, L., et al. 2017, *Science*, **355**, 817
- Jadhav, S., Mukund, N., Gadre, B., Mitra, S., & Abraham, S. 2021, *Phys. Rev. D*, **104**, 064051
- Jani, K., Healy, J., Clark, J. A., et al. 2016, *Class. Quant. Grav.*, **33**, 204001
- Jani, K., Shoemaker, D., & Cutler, C. 2020, *Nat. Astron.*, **4**, 260
- Kaaret, P., Prestwich, A. H., Zezas, A., et al. 2001, *MNRAS*, **321**, L29
- Kaaret, P., Feng, H., & Roberts, T. P. 2017, *ARA&A*, **55**, 303
- Kamaretsos, I., Hannam, M., Husa, S., & Sathyaprakash, B. S. 2012, *Phys. Rev. D*, **85**, 024018
- Kimball, C., Talbot, C., Berry, C. P. L., et al. 2021, *ApJ*, **915**, L35
- King, A. R., & Dehnen, W. 2005, *MNRAS*, **357**, 275
- Kızıltan, B., Baumgardt, H., & Loeb, A. 2017, *Nature*, **542**, 203
- Klimenko, S., & Mitselmakher, G. 2004, *Class. Quant. Grav.*, **21**, S1819
- Klimenko, S., Mohanty, S., Rakhmanov, M., & Mitselmakher, G. 2005, *Phys. Rev. D*, **72**, 122002
- Klimenko, S., Mohanty, S., Rakhmanov, M., & Mitselmakher, G. 2006, *J. Phys. Conf. Ser.*, **32**, 12
- Klimenko, S., Vedovato, G., Drago, M., et al. 2011, *Phys. Rev. D*, **83**, 102001
- Klimenko, S., Vedovato, G., Drago, M., et al. 2016, *Phys. Rev. D*, **93**, 042004
- Koliopoulos, F. 2017, *Proceedings of the XII Multifrequency Behaviour of High Energy Cosmic Sources Workshop*, 12–17 June, 51
- Kormendy, J., & Ho, L. C. 2013, *ARA&A*, **51**, 511
- Kremer, K., Spera, M., Becker, D., et al. 2020, *ApJ*, **903**, 45
- Lange, J., O'Shaughnessy, R., Boyle, M., et al. 2017, *Phys. Rev. D*, **96**, 104041
- Lanzoni, B., Mucciarelli, A., Origlia, L., et al. 2013, *ApJ*, **769**, 107
- Lin, D., Strader, J., Carrasco, E. R., et al. 2018, *Nat. Astron.*, **2**, 656
- Littenberg, T. B., Kanner, J. B., Cornish, N. J., & Millhouse, M. 2016, *Phys. Rev. D*, **94**, 044050
- Lützgendorf, N., Kissler-Patig, M., Noyola, E., et al. 2011, *A&A*, **533**, A36
- Madau, P., & Rees, M. J. 2001, *ApJ*, **551**, L27
- Mapelli, M. 2016, *MNRAS*, **459**, 3432
- Mapelli, M., Spera, M., Montanari, E., et al. 2020, *ApJ*, **888**, 76
- Mapelli, M., Dall'Amico, M., Bouffanais, Y., et al. 2021, *MNRAS*, **505**, 339
- Marchant, P., & Moriya, T. J. 2020, *A&A*, **640**, L18
- McKernan, B., Ford, K. E. S., Lyra, W., & Perets, H. B. 2012, *MNRAS*, **425**, 460
- McKernan, B., Ford, K. E. S., Bellovary, J., et al. 2018, *ApJ*, **866**, 66
- Meidam, J., Agathos, M., Van Den Broeck, C., Veitch, J., & Sathyaprakash, B. S. 2014, *Phys. Rev. D*, **90**, 064009
- Messick, C., Blackburn, K., Brady, P., et al. 2017, *Phys. Rev. D*, **95**, 042001
- Mezcua, M. 2017, *Int. J. Mod. Phys. D*, **26**, 1730021
- Miller, M. C. 2009, *Class. Quant. Grav.*, **26**, 094031
- Miller, M. C., & Colbert, E. J. M. 2004, *Int. J. Mod. Phys. D*, **13**, 1
- Miller, M. C., & Hamilton, D. P. 2002, *MNRAS*, **330**, 232
- Mozzon, S., Nuttall, L. K., Lundgren, A., et al. 2020, *Class. Quant. Grav.*, **37**, 215014
- Mroué, A. H., Scheel, M. A., Szilágyi, B., et al. 2013, *Phys. Rev. Lett.*, **111**, 241104
- Necula, V., Klimenko, S., & Mitselmakher, G. 2012, *J. Phys. Conf. Ser.*, **363**, 012032
- Nguyen, P., Schofield, R. M. S., Effler, A., et al. 2021, *Class. Quant. Grav.*, **38**, 145001
- Nitz, A. H. 2018, *Class. Quant. Grav.*, **35**, 035016
- Nitz, A. H., & Capano, C. D. 2021, *ApJ*, **907**, L9
- Nitz, A. H., Dent, T., Dal Canton, T., Fairhurst, S., & Brown, D. A. 2017, *ApJ*, **849**, 118
- Nitz, A. H., Dent, T., Davies, G. S., et al. 2019, *ApJ*, **891**, 123
- Noyola, E., Gebhardt, K., & Bergmann, M. 2008, *ApJ*, **676**, 1008
- O'Leary, R. M., Rasio, F. A., Fregeau, J. M., Ivanova, N., & O'Shaughnessy, R. 2006, *ApJ*, **637**, 937

- Ossokine, S., Buonanno, A., Marsat, S., et al. 2020, *Phys. Rev. D*, **102**, 044055
 Owen, B. J. 1996, *Phys. Rev. D*, **53**, 6749
- Pankow, C., Chatzioannou, K., Chase, E. A., et al. 2018, *Phys. Rev. D*, **98**, 084016
 Pasham, D. R., Strohmayer, T. E., & Mushotzky, R. F. 2015, *Nature*, **513**, 74
 Paynter, J., Webster, R., & Thrane, E. 2021, *Nat. Astron.*, **5**, 560
 Planck Collaboration XIII. 2016, *A&A*, **594**, A13
 Pratten, G., García-Quiros, C., Colleoni, M., et al. 2021, *Phys. Rev. D*, **103**, 104056
 Pürer, M. 2016, *Phys. Rev. D*, **93**, 064041
 Rasskazov, A., Fragione, G., & Kocsis, B. 2020, *ApJ*, **899**, 149
 Remillard, R. A., & McClintock, J. E. 2006, *ARA&A*, **44**, 49
 Renzo, M., Cantiello, M., Metzger, B. D., & Jiang, Y. F. 2020a, *ApJ*, **904**, L13
 Renzo, M., Farmer, R. J., Justham, S., et al. 2020b, *MNRAS*, **493**, 4333
 Rice, J. R., & Zhang, B. 2021, *ApJ*, **908**, 59
 Rodriguez, C. L., Zevin, M., Amaro-Seoane, P., et al. 2019, *Phys. Rev. D*, **100**, 043027
 Romero-Shaw, I., Lasky, P. D., Thrane, E., & Calderón Bustillo, J. 2020, *ApJ*, **903**, L5
 Roupas, Z., & Kazanas, D. 2019, *A&A*, **632**, L8
 Sachdev, S., Caudill, S., Fong, H., et al. 2019, Phys. Rev. D, submitted [arXiv:1901.08580]
 Safarzadeh, M., & Haiman, Z. 2020, *ApJ*, **903**, L21
 Salemi, F., Miliotti, E., Prodi, G. A., et al. 2019, *Phys. Rev. D*, **100**, 042003
 Sathyaprakash, B. S., & Dhurandhar, S. V. 1991, *Phys. Rev. D*, **44**, 3819
 Sathyaprakash, B. S., & Schutz, B. F. 2009, *Liv. Rev. Relativ.*, **12**, 2
 Schmidt, P., Ohme, F., & Hannam, M. 2015, *Phys. Rev. D*, **91**, 024043
 Servillat, M., Farrell, S. A., Lin, D., et al. 2011, *ApJ*, **743**, 6
 Soni, S., Berry, C. P. L., Coughlin, S. B., et al. 2021, *Class. Quant. Grav.*, **38**, 19
 Soria, R., Hakala, P. J., Hau, G. K. T., Gladstone, J. C., & Kong, A. K. H. 2012, *MNRAS*, **420**, 3599
 Spera, M., & Mapelli, M. 2017, *MNRAS*, **470**, 4739
 Stevenson, S., Sampson, M., Powell, J., et al. 2019, *ApJ*, **882**, 121
 Sun, L., Goetz, E., Kissel, J. S., et al. 2020, *Class. Quant. Grav.*, **37**, 225008
 Szczepańczyk, M., Klimenko, S., O'Brien, B., et al. 2021, *Phys. Rev. D*, **103**, 082002
 Tagawa, H., Haiman, Z., Bartos, I., & Kocsis, B. 2020, *ApJ*, **899**, 26
 Tagawa, H., Kocsis, B., Haiman, Z., et al. 2021, *ApJ*, **908**, 194
 Tanikawa, A., Kinugawa, T., Yoshida, T., Hijikawa, K., & Umeda, H. 2021, *MNRAS*, **505**, 2170
 Thrane, E., Lasky, P. D., & Levin, Y. 2017, *Phys. Rev. D*, **96**, 102004
 Tiwari, V., Fairhurst, S., & Hannam, M. 2018, *ApJ*, **868**, 140
 Umeda, H., Yoshida, T., Nagele, C., & Takahashi, K. 2020, *ApJ*, **905**, L21
 Usman, S. A., Nitz, A. H., Harry, I. W., et al. 2016, *Class. Quant. Grav.*, **33**, 215004
 Vajente, G., Huang, Y., Isi, M., et al. 2020, *Phys. Rev. D*, **101**, 042003
 van den Bosch, R., de Zeeuw, T., Gebhardt, K., Noyola, E., & van de Ven, G. 2006, *ApJ*, **641**, 852
 van der Marel, R. P. 2004, *Coevolution of Black Holes and Galaxies* (Cambridge: Cambridge University Press), 37
 van Son, L. A. C., De Mink, S. E., Broekgaarden, F. S., et al. 2020, *ApJ*, **897**, 100
 Varma, V., Field, S. E., Scheel, M. A., et al. 2019, *Phys. Rev. Res.*, **1**, 033015
 Veitch, J., & Vecchio, A. 2008, *Phys. Rev. D*, **78**, 022001
 Veitch, J., Raymond, V., Farr, B., et al. 2015, *Phys. Rev. D*, **91**, 042003
 Viets, A., Wade, M., Urban, A. L., et al. 2018, *Class. Quant. Grav.*, **35**, 095015
 Vink, J. S., Higgins, E. R., Sander, A. A. C., & Sabhahit, G. N. 2021, *MNRAS*, **504**, 146
 Vitral, E., & Mamon, G. A. 2021, *A&A*, **646**, A63
 Volonteri, M. 2010, *A&ARv*, **18**, 279
 Webb, N., Cseh, D., Lenc, E., et al. 2012, *Science*, **337**, 554
 Woosley, S. E. 2017, *ApJ*, **836**, 244
 Woosley, S. E. 2019, *ApJ*, **878**, 49
 Woosley, S. E., & Heger, A. 2021, *ApJ*, **912**, L31
 Woosley, S. E., Blinnikov, S., & Heger, A. 2007, *Nature*, **450**, 390
 Wysocki, D., O'Shaughnessy, R., Lange, J., & Fang, Y.-L. L. 2019, *Phys. Rev. D*, **99**, 084026
 Yang, Y., Bartos, I., Gayathri, V., et al. 2019, *Phys. Rev. Lett.*, **123**, 181101
 Yunes, N., & Siemens, X. 2013, *Liv. Rev. Relativ.*, **16**, 9
 Yunes, N., Yagi, K., & Pretorius, F. 2016, *Phys. Rev. D*, **94**, 084002
- ¹ LIGO Laboratory, California Institute of Technology, Pasadena, CA 91125, USA
² Louisiana State University, Baton Rouge, LA 70803, USA
³ Dipartimento di Farmacia, Università di Salerno, 84084 Fisciano, Salerno, Italy
- ⁴ INFN, Sezione di Napoli, Complesso Universitario di Monte S. Angelo, 80126 Napoli, Italy
⁵ OzGrav, School of Physics and Astronomy, Monash University, Clayton 3800, Victoria, Australia
⁶ LIGO Livingston Observatory, Livingston, LA 70754, USA
⁷ University of Wisconsin-Milwaukee, Milwaukee, WI 53201, USA
⁸ OzGrav, Australian National University, Canberra, ACT 0200, Australia
⁹ Max Planck Institute for Gravitational Physics (Albert Einstein Institute), 30167 Hannover, Germany
¹⁰ Leibniz Universität Hannover, 30167 Hannover, Germany
¹¹ Inter-University Centre for Astronomy and Astrophysics, Pune 411007, India
¹² University of Cambridge, Cambridge CB2 1TN, UK
¹³ Theoretisch-Physikalisches Institut, Friedrich-Schiller-Universität Jena, 07743 Jena, Germany
¹⁴ University of Birmingham, Birmingham B15 2TT, UK
¹⁵ Center for Interdisciplinary Exploration and Research in Astrophysics (CIERA), Northwestern University, Evanston, IL 60208, USA
¹⁶ Instituto Nacional de Pesquisas Espaciais, 12227-010 São José dos Campos, São Paulo, Brazil
¹⁷ Gravity Exploration Institute, Cardiff University, Cardiff CF24 3AA, UK
¹⁸ INFN, Sezione di Pisa, 56127 Pisa, Italy
¹⁹ International Centre for Theoretical Sciences, Tata Institute of Fundamental Research, Bengaluru 560089, India
²⁰ Gravitational Wave Science Project, National Astronomical Observatory of Japan (NAOJ), Mitaka, Tokyo 181-8588, Japan
²¹ Advanced Technology Center, National Astronomical Observatory of Japan (NAOJ), Mitaka, Tokyo 181-8588, Japan
²² INFN Sezione di Torino, 10125 Torino, Italy
²³ Università di Napoli “Federico II”, Complesso Universitario di Monte S. Angelo, 80126 Napoli, Italy
²⁴ Université de Lyon, Université Claude Bernard Lyon 1, CNRS, Institut Lumière Matière, 69622 Villeurbanne, France
²⁵ Department of Physics, The University of Tokyo, Bunkyo-ku, Tokyo 113-0033, Japan
²⁶ Research Center for the Early Universe (RESCEU), The University of Tokyo, Bunkyo-ku, Tokyo 113-0033, Japan
²⁷ Institut de Ciències del Cosmos (ICCUB), Universitat de Barcelona, C/Martí i Franquès 1, Barcelona 08028, Spain
²⁸ Laboratoire d’Annecy de Physique des Particules (LAPP), Univ. Grenoble Alpes, Université Savoie Mont Blanc, CNRS/IN2P3, 74941 Annecy, France
²⁹ Gran Sasso Science Institute (GSSI), 67100, L’Aquila, Italy, SUPA, University of Strathclyde, Glasgow G1 1XQ, UK
³⁰ Dipartimento di Scienze Matematiche, Informatiche e Fisiche, Università di Udine, 33100 Udine, Italy
³¹ INFN, Sezione di Trieste, 34127 Trieste, Italy
³² Embry-Riddle Aeronautical University, Prescott, AZ 86301, USA
³³ Université de Paris, CNRS, Astroparticule et Cosmologie, 75006 Paris, France
³⁴ Institute for Cosmic Ray Research (ICRR), KAGRA Observatory, The University of Tokyo, Kashiwa, Chiba 277-8582, Japan
³⁵ Accelerator Laboratory, High Energy Accelerator Research Organization (KEK), Tsukuba, Ibaraki 305-0801, Japan
³⁶ Earthquake Research Institute, The University of Tokyo, Bunkyo-ku, Tokyo 113-0032, Japan
³⁷ California State University Fullerton, Fullerton, CA 92831, USA
³⁸ Université Paris-Saclay, CNRS/IN2P3, IJCLab, 91405 Orsay, France
³⁹ European Gravitational Observatory (EGO), 56021 Cascina, Pisa, Italy
⁴⁰ Chennai Mathematical Institute, Chennai 603103, India
⁴¹ Department of Mathematics and Physics, Gravitational Wave Science Project, Hirosaki University, Hirosaki, Aomori 036-8561, Japan
⁴² Columbia University, New York, NY 10027, USA

- ⁴³ Kamioka Branch, National Astronomical Observatory of Japan (NAOJ), Kamioka-cho, Hida, Gifu 506-1205, Japan
- ⁴⁴ The Graduate University for Advanced Studies (SOKENDAI), Mitaka, Tokyo 181-8588, Japan
- ⁴⁵ Università degli Studi di Urbino “Carlo Bo”, 61029 Urbino, Italy
- ⁴⁶ INFN, Sezione di Firenze, 50019 Sesto Fiorentino, Firenze, Italy
- ⁴⁷ INFN, Sezione di Roma, 00185 Roma, Italy
- ⁴⁸ Université catholique de Louvain, 1348 Louvain-la-Neuve, Belgium
- ⁴⁹ Nikhef, Science Park 105, 1098 XG Amsterdam, The Netherlands
- ⁵⁰ King’s College London, University of London, London WC2R 2LS, UK
- ⁵¹ Korea Institute of Science and Technology Information (KISTI), Yuseong-gu, Daejeon 34141, Korea
- ⁵² National Institute for Mathematical Sciences, Yuseong-gu, Daejeon 34047, Korea
- ⁵³ Christopher Newport University, Newport News, VA 23606, USA
- ⁵⁴ International College, Osaka University, Toyonaka, Osaka 560-0043, Japan
- ⁵⁵ School of High Energy Accelerator Science, The Graduate University for Advanced Studies (SOKENDAI), Tsukuba, Ibaraki 305-0801, Japan
- ⁵⁶ University of Oregon, Eugene, OR 97403, USA
- ⁵⁷ Syracuse University, Syracuse, NY 13244, USA
- ⁵⁸ Université de Liège, 4000 Liège, Belgium
- ⁵⁹ University of Minnesota, Minneapolis, MN 55455, USA
- ⁶⁰ Università degli Studi di Milano-Bicocca, 20126 Milano, Italy
- ⁶¹ INFN, Sezione di Milano-Bicocca, 20126 Milano, Italy
- ⁶² INAF, Osservatorio Astronomico di Brera sede di Merate, 23807 Merate, Lecco, Italy
- ⁶³ LIGO Hanford Observatory, Richland, WA 99352, USA
- ⁶⁴ Dipartimento di Medicina, Chirurgia e Odontoiatria “Scuola Medica Salernitana”, Università di Salerno, 84081 Baronissi, Salerno, Italy
- ⁶⁵ SUPA, University of Glasgow, Glasgow G12 8QQ, UK
- ⁶⁶ LIGO Laboratory, Massachusetts Institute of Technology, Cambridge, MA 02139, USA
- ⁶⁷ Wigner RCP, RMKI, Konkoly Thege Miklós út 29-33, 1121 Budapest, Hungary
- ⁶⁸ University of Florida, Gainesville, FL 32611, USA
- ⁶⁹ Stanford University, Stanford, CA 94305, USA
- ⁷⁰ Università di Pisa, 56127 Pisa, Italy
- ⁷¹ INFN, Sezione di Perugia, 06123 Perugia, Italy
- ⁷² Università di Perugia, 06123 Perugia, Italy
- ⁷³ Università di Padova, Dipartimento di Fisica e Astronomia, 35131 Padova, Italy
- ⁷⁴ INFN, Sezione di Padova, 35131 Padova, Italy
- ⁷⁵ Montana State University, Bozeman, MT 59717, USA
- ⁷⁶ Institute for Plasma Research, Bhat, Gandhinagar 382428, India
- ⁷⁷ Nicolaus Copernicus Astronomical Center, Polish Academy of Sciences, 00-716 Warsaw, Poland
- ⁷⁸ Dipartimento di Ingegneria, Università del Sannio, 82100 Benevento, Italy
- ⁷⁹ OzGrav, University of Adelaide, Adelaide, South Australia 5005, Australia
- ⁸⁰ California State University, Los Angeles, 5151 State University Dr, Los Angeles, CA 90032, USA
- ⁸¹ INFN, Sezione di Genova, 16146 Genova, Italy
- ⁸² OzGrav, University of Western Australia, Crawley, Western Australia 6009, Australia
- ⁸³ RRCAT, Indore, Madhya Pradesh 452013, India
- ⁸⁴ GRAPPA, Anton Pannekoek Institute for Astronomy and Institute for High-Energy Physics, University of Amsterdam, Science Park 904, 1098 XH Amsterdam, The Netherlands
- ⁸⁵ Missouri University of Science and Technology, Rolla, MO 65409, USA
- ⁸⁶ Faculty of Physics, Lomonosov Moscow State University, Moscow 119991, Russia
- ⁸⁷ Università di Trento, Dipartimento di Fisica, 38123 Povo, Trento, Italy
- ⁸⁸ INFN, Trento Institute for Fundamental Physics and Applications, 38123 Povo, Trento, Italy
- ⁸⁹ SUPA, University of the West of Scotland, Paisley PA1 2BE, UK
- ⁹⁰ Bar-Ilan University, Ramat Gan 5290002, Israel
- ⁹¹ Artemis, Université Côte d’Azur, Observatoire de la Côte d’Azur, CNRS, 06304 Nice, France
- ⁹² Dipartimento di Fisica “E.R. Caianiello”, Università di Salerno, 84084 Fisciano, Salerno, Italy
- ⁹³ INFN, Sezione di Napoli, Gruppo Collegato di Salerno, Complesso Universitario di Monte S. Angelo, 80126 Napoli, Italy
- ⁹⁴ Università di Roma “La Sapienza”, 00185 Roma, Italy
- ⁹⁵ Univ. Rennes, CNRS, Institut FOTON – UMR6082, 3500 Rennes, France
- ⁹⁶ Indian Institute of Technology Bombay, Powai, Mumbai 400 076, India
- ⁹⁷ INFN, Laboratori Nazionali del Gran Sasso, 67100 Assergi, Italy
- ⁹⁸ Laboratoire Kastler Brossel, Sorbonne Université, CNRS, ENS-Université PSL, Collège de France, 75005 Paris, France
- ⁹⁹ Astronomical Observatory Warsaw University, 00-478 Warsaw, Poland
- ¹⁰⁰ University of Maryland, College Park, MD 20742, USA
- ¹⁰¹ Max Planck Institute for Gravitational Physics (Albert Einstein Institute), 14476 Potsdam, Germany
- ¹⁰² L2IT, Laboratoire des 2 Infinis – Toulouse, Université de Toulouse, CNRS/IN2P3, UPS, 31062 Toulouse Cedex 9, France
- ¹⁰³ School of Physics, Georgia Institute of Technology, Atlanta, GA 30332, USA
- ¹⁰⁴ IGFAE, Campus Sur, Universidade de Santiago de Compostela, 15782 Santiago de Compostela, Spain
- ¹⁰⁵ The Chinese University of Hong Kong, Shatin, NT, Hong Kong
- ¹⁰⁶ Stony Brook University, Stony Brook, NY 11794, USA
- ¹⁰⁷ Center for Computational Astrophysics, Flatiron Institute, New York, NY 10010, USA
- ¹⁰⁸ NASA Goddard Space Flight Center, Greenbelt, MD 20771, USA
- ¹⁰⁹ Dipartimento di Fisica, Università degli Studi di Genova, 16146 Genova, Italy
- ¹¹⁰ Institute for Gravitational and Subatomic Physics (GRASP), Utrecht University, Princetonplein 1, 3584 CC Utrecht, The Netherlands
- ¹¹¹ RESCEU, University of Tokyo, Tokyo 113-0033, Japan
- ¹¹² Department of Astronomy, Beijing Normal University, Beijing 100875, PR China
- ¹¹³ OzGrav, University of Melbourne, Parkville, Victoria 3010, Australia
- ¹¹⁴ Università degli Studi di Sassari, 07100 Sassari, Italy
- ¹¹⁵ INFN, Laboratori Nazionali del Sud, 95125 Catania, Italy
- ¹¹⁶ Università di Roma Tor Vergata, 00133 Roma, Italy
- ¹¹⁷ INFN, Sezione di Roma Tor Vergata, 00133 Roma, Italy
- ¹¹⁸ University of Sannio at Benevento, 82100, Benevento, Italy and INFN, Sezione di Napoli, 80100 Napoli, Italy
- ¹¹⁹ Villanova University, 800 Lancaster Ave, Villanova, PA 19085, USA
- ¹²⁰ Departamento de Astronomía y Astrofísica, Universitat de València, 46100 Burjassot, València, Spain
- ¹²¹ Universität Hamburg, 22761 Hamburg, Germany
- ¹²² Rochester Institute of Technology, Rochester, NY 14623, USA
- ¹²³ National Tsing Hua University, Hsinchu 30013, Taiwan
- ¹²⁴ Department of Applied Physics, Fukuoka University, Jonan, Fukuoka, Fukuoka 814-0180, Japan
- ¹²⁵ OzGrav, Charles Sturt University, Wagga Wagga, New South Wales 2678, Australia
- ¹²⁶ Department of Physics, Tamkang University, Danshui Dist., New Taipei 25137, Taiwan
- ¹²⁷ Department of Physics and Institute of Astronomy, National Tsing Hua University, Hsinchu 30013, Taiwan
- ¹²⁸ Department of Physics, Center for High Energy and High Field Physics, National Central University, Zhongli, Taoyuan 32001, Taiwan
- ¹²⁹ CaRT, California Institute of Technology, Pasadena, CA 91125, USA

- ¹³⁰ Department of Physics, National Tsing Hua University, Hsinchu 30013, Taiwan
- ¹³¹ Dipartimento di Ingegneria Industriale (DIIN), Università di Salerno, 84084 Fisciano, Salerno, Italy
- ¹³² Institute of Physics, Academia Sinica, Nankang, Taipei 11529, Taiwan
- ¹³³ Université Lyon, Université Claude Bernard Lyon 1, CNRS, IP2I Lyon/IN2P3, UMR 5822, 69622 Villeurbanne, France
- ¹³⁴ Seoul National University, Seoul 08826, South Korea
- ¹³⁵ Pusan National University, Busan 46241, South Korea
- ¹³⁶ INAF, Osservatorio Astronomico di Padova, 35122 Padova, Italy
- ¹³⁷ University of Arizona, Tucson, AZ 85721, USA
- ¹³⁸ Rutherford Appleton Laboratory, Didcot OX11 0DE, UK
- ¹³⁹ OzGrav, Swinburne University of Technology, Hawthorn, VIC 3122, Australia
- ¹⁴⁰ Université Libre de Bruxelles, Avenue Franklin Roosevelt 50, 1050 Bruxelles, Belgium
- ¹⁴¹ Universitat de les Illes Balears, IAC3–IEEC, 07122 Palma de Mallorca, Spain
- ¹⁴² Université Libre de Bruxelles, Brussels 1050, Belgium
- ¹⁴³ Departamento de Matemáticas, Universitat de València, 46100 Burjassot, València, Spain
- ¹⁴⁴ Texas Tech University, Lubbock, TX 79409, USA
- ¹⁴⁵ The Pennsylvania State University, University Park, PA 16802, USA
- ¹⁴⁶ University of Rhode Island, Kingston, RI 02881, USA
- ¹⁴⁷ The University of Texas Rio Grande Valley, Brownsville, TX 78520, USA
- ¹⁴⁸ Bellevue College, Bellevue, WA 98007, USA
- ¹⁴⁹ Scuola Normale Superiore, Piazza dei Cavalieri, 7, 56126 Pisa, Italy
- ¹⁵⁰ MTA-ELTE Astrophysics Research Group, Institute of Physics, Eötvös University, Budapest 1117, Hungary
- ¹⁵¹ Maastricht University, PO Box 616, 6200 MD Maastricht, The Netherlands
- ¹⁵² University of Portsmouth, Portsmouth PO1 3FX, UK
- ¹⁵³ The University of Sheffield, Sheffield S10 2TN, UK
- ¹⁵⁴ Université Lyon, Université Claude Bernard Lyon 1, CNRS, Laboratoire des Matériaux Avancés (LMA), IP2I Lyon/IN2P3, UMR 5822, 69622 Villeurbanne, France
- ¹⁵⁵ Dipartimento di Scienze Matematiche, Fisiche e Informatiche, Università di Parma, 43124 Parma, Italy
- ¹⁵⁶ INFN, Sezione di Milano Bicocca, Gruppo Collegato di Parma, 43124 Parma, Italy
- ¹⁵⁷ Physik-Institut, University of Zurich, Winterthurerstrasse 190, 8057 Zurich, Switzerland
- ¹⁵⁸ University of Chicago, Chicago, IL 60637, USA
- ¹⁵⁹ Université de Strasbourg, CNRS, IPHC UMR 7178, 67000 Strasbourg, France
- ¹⁶⁰ West Virginia University, Morgantown, WV 26506, USA
- ¹⁶¹ Montclair State University, Montclair, NJ 07043, USA
- ¹⁶² Colorado State University, Fort Collins, CO 80523, USA
- ¹⁶³ Institute for Nuclear Research, Hungarian Academy of Sciences, Bem t'er 18/c, 4026 Debrecen, Hungary
- ¹⁶⁴ Department of Physics, University of Texas, Austin, TX 78712, USA
- ¹⁶⁵ CNR-SPIN, c/o Università di Salerno, 84084 Fisciano, Salerno, Italy
- ¹⁶⁶ Scuola di Ingegneria, Università della Basilicata, 85100 Potenza, Italy
- ¹⁶⁷ Gravitational Wave Science Project, National Astronomical Observatory of Japan (NAOJ), Mitaka, Tokyo 181-8588, Japan
- ¹⁶⁸ Observatori Astronòmic, Universitat de València, 46980 Paterna València, Spain
- ¹⁶⁹ The University of Utah, Salt Lake, UT 84112, USA
- ¹⁷⁰ Kenyon College, Gambier, OH 43022, USA
- ¹⁷¹ Vrije Universiteit Amsterdam, 1081 HV Amsterdam, The Netherlands
- ¹⁷² Department of Astronomy, The University of Tokyo, Mitaka, Tokyo 181-8588, Japan
- ¹⁷³ Faculty of Engineering, Niigata University, Nishi-ku, Niigata, Niigata 950-2181, Japan
- ¹⁷⁴ State Key Laboratory of Magnetic Resonance and Atomic and Molecular Physics, Innovation Academy for Precision Measurement Science and Technology (APM), Chinese Academy of Sciences, Xiao Hong Shan, Wuhan 430071, PR China
- ¹⁷⁵ University of Szeged, Dóm tér 9, Szeged 6720, Hungary
- ¹⁷⁶ Universiteit Gent, 9000 Gent, Belgium
- ¹⁷⁷ Cornell University, Ithaca, NY 14850, USA
- ¹⁷⁸ University of British Columbia, Vancouver, BC V6T 1Z4, Canada
- ¹⁷⁹ Tata Institute of Fundamental Research, Mumbai 400005, India
- ¹⁸⁰ INAF, Osservatorio Astronomico di Capodimonte, 80131 Napoli, Italy
- ¹⁸¹ The University of Mississippi, University, Mississippi, MS 38677, USA
- ¹⁸² University of Michigan, Ann Arbor, MI 48109, USA
- ¹⁸³ Texas A&M University, College Station, TX 77843, USA
- ¹⁸⁴ Department of Physics, Ulsan National Institute of Science and Technology (UNIST), Ulju-gun, Ulsan 44919, Korea
- ¹⁸⁵ Applied Research Laboratory, High Energy Accelerator Research Organization (KEK), Tsukuba, Ibaraki 305-0801, Japan
- ¹⁸⁶ Dipartimento di Fisica, Università di Trieste, 34127 Trieste, Italy
- ¹⁸⁷ Shanghai Astronomical Observatory, Chinese Academy of Sciences, Shanghai 200030, PR China
- ¹⁸⁸ American University, Washington, DC 20016, USA
- ¹⁸⁹ Faculty of Science, University of Toyama, Toyama, Toyama 930-8555, Japan
- ¹⁹⁰ Institute for Cosmic Ray Research (ICRR), KAGRA Observatory, The University of Tokyo, Kamioka-cho, Hida, Gifu 506-1205, Japan
- ¹⁹¹ Carleton College, Northfield, MN 55057, USA
- ¹⁹² University of California, Berkeley, CA 94720, USA
- ¹⁹³ Maastricht University, 6200 MD Maastricht, The Netherlands
- ¹⁹⁴ College of Industrial Technology, Nihon University, Narashino, Chiba 275-8575, Japan
- ¹⁹⁵ Graduate School of Science and Technology, Niigata University, Nishi-ku, Niigata, Niigata 950-2181, Japan
- ¹⁹⁶ Department of Physics, National Taiwan Normal University, Sec. 4, Taipei 116, Taiwan
- ¹⁹⁷ Astronomy & Space Science, Chungnam National University, Yuseong-gu, Daejeon 34134, Korea
- ¹⁹⁸ Department of Physics and Mathematics, Aoyama Gakuin University, Sagamihara, Kanagawa 252-5258, Japan
- ¹⁹⁹ Kavli Institute for Astronomy and Astrophysics, Peking University, Haidian, Beijing 100871, PR China
- ²⁰⁰ Yukawa Institute for Theoretical Physics (YITP), Kyoto University, Sakyou-ku, Kyoto, Kyoto 606-8502, Japan
- ²⁰¹ Graduate School of Science and Engineering, University of Toyama, Toyama, Toyama 930-8555, Japan
- ²⁰² Department of Physics, Graduate School of Science, Osaka City University, Sumiyoshi-ku, Osaka, Osaka 558-8585, Japan
- ²⁰³ Nambu Yoichiro Institute of Theoretical and Experimental Physics (NITEP), Osaka City University, Sumiyoshi-ku, Osaka, Osaka 558-8585, Japan
- ²⁰⁴ Institute of Space and Astronautical Science (JAXA), Chuo-ku, Sagamihara, Kanagawa 252-0222, Japan
- ²⁰⁵ Directorate of Construction, Services & Estate Management, Mumbai 400094, India
- ²⁰⁶ Vanderbilt University, Nashville, TN 37235, USA
- ²⁰⁷ Universiteit Antwerpen, Prinsstraat 13, 2000 Antwerpen, Belgium
- ²⁰⁸ University of Białystok, 15-424 Białystok, Poland
- ²⁰⁹ Department of Physics, Ewha Womans University, Seodaemun-gu, Seoul 03760, Korea
- ²¹⁰ National Astronomical Observatories, Chinese Academic of Sciences, Chaoyang, Beijing, PR China
- ²¹¹ School of Astronomy and Space Science, University of Chinese Academy of Sciences, Chaoyang, Beijing, PR China
- ²¹² University of Southampton, Southampton SO17 1BJ, UK
- ²¹³ Institute for Cosmic Ray Research (ICRR), The University of Tokyo, Kashiwa, Chiba 277-8582, Japan

- ²¹⁴ Faculty of Science, University of Toyama, Toyama, Toyama 930-8555, Japan
- ²¹⁵ Chung-Ang University, Seoul 06974, South Korea
- ²¹⁶ Institut de Física d'Altes Energies (IFAE), Barcelona Institute of Science and Technology, and ICREA, 08193 Barcelona, Spain
- ²¹⁷ Graduate School of Science, Tokyo Institute of Technology, Meguro-ku, Tokyo 152-8551, Japan
- ²¹⁸ University of Washington Bothell, Bothell, WA 98011, USA
- ²¹⁹ Institute of Applied Physics, Nizhny Novgorod 603950, Russia
- ²²⁰ Ewha Womans University, Seoul 03760, South Korea
- ²²¹ Inje University Gimhae, South Gyeongsang 50834, South Korea
- ²²² Department of Physics, Myongji University, Yongin 17058, Korea
- ²²³ Korea Astronomy and Space Science Institute, Daejeon 34055, South Korea
- ²²⁴ National Institute for Mathematical Sciences, Daejeon 34047, South Korea
- ²²⁵ Ulsan National Institute of Science and Technology, Ulsan 44919, South Korea
- ²²⁶ Department of Physical Science, Hiroshima University, Higashihiroshima, Hiroshima 903-0213, Japan
- ²²⁷ School of Physics and Astronomy, Cardiff University, Cardiff CF24 3AA, UK
- ²²⁸ Institute of Astronomy, National Tsing Hua University, Hsinchu 30013, Taiwan
- ²²⁹ Bard College, 30 Campus Rd, Annandale-On-Hudson, NY 12504, USA
- ²³⁰ Institute of Mathematics, Polish Academy of Sciences, 00656 Warsaw, Poland
- ²³¹ National Center for Nuclear Research, 05-400 Świerk-Otwock, Poland
- ²³² Instituto de Fisica Teorica, 28049 Madrid, Spain
- ²³³ Department of Physics, Nagoya University, Chikusa-ku, Nagoya, Aichi 464-8602, Japan
- ²³⁴ Université de Montréal/Polytechnique, Montreal, Quebec H3T 1J4, Canada
- ²³⁵ Laboratoire Lagrange, Université Côte d'Azur, Observatoire Côte d'Azur, CNRS, 06304 Nice, France
- ²³⁶ Department of Physics, Hanyang University, Seoul 04763, Korea
- ²³⁷ Sungkyunkwan University, Seoul 03063, South Korea
- ²³⁸ NAVIER, École des Ponts, Univ. Gustave Eiffel, CNRS, Marne-la-Vallée, France
- ²³⁹ Department of Physics, National Cheng Kung University, Tainan 701, Taiwan
- ²⁴⁰ National Center for High-performance computing, National Applied Research Laboratories, Hsinchu Science Park, Hsinchu 30076, Taiwan
- ²⁴¹ Institute for High-Energy Physics, University of Amsterdam, Science Park 904, 1098 XH Amsterdam, The Netherlands
- ²⁴² NASA Marshall Space Flight Center, Huntsville, AL 35811, USA
- ²⁴³ University of Washington, Seattle, WA 98195, USA
- ²⁴⁴ Dipartimento di Matematica e Fisica, Università degli Studi Roma Tre, 00146 Roma, Italy
- ²⁴⁵ INFN, Sezione di Roma Tre, 00146 Roma, Italy
- ²⁴⁶ ESPCI, CNRS, 75005 Paris, France
- ²⁴⁷ Concordia University Wisconsin, Mequon, WI 53097, USA
- ²⁴⁸ Università di Camerino, Dipartimento di Fisica, 62032 Camerino, Italy
- ²⁴⁹ School of Physics Science and Engineering, Tongji University, Shanghai 200092, PR China
- ²⁵⁰ Southern University and A&M College, Baton Rouge, LA 70813, USA
- ²⁵¹ Centre Scientifique de Monaco, 8 Quai Antoine Ier, 98000, Monaco
- ²⁵² Institute for Photon Science and Technology, The University of Tokyo, Bunkyo-ku, Tokyo 113-8656, Japan
- ²⁵³ Indian Institute of Technology Madras, Chennai 600036, India
- ²⁵⁴ Saha Institute of Nuclear Physics, Bidhannagar, West Bengal 700064, India
- ²⁵⁵ The Applied Electromagnetic Research Institute, National Institute of Information and Communications Technology (NICT), Koganei, Tokyo 184-8795, Japan
- ²⁵⁶ Institut des Hautes Etudes Scientifiques, 91440 Bures-sur-Yvette, France
- ²⁵⁷ Faculty of Law, Ryukoku University, Fushimi-ku, Kyoto, Kyoto 612-8577, Japan
- ²⁵⁸ Indian Institute of Science Education and Research, Kolkata, Mohanpur, West Bengal 741252, India
- ²⁵⁹ Department of Astrophysics/IMAPP, Radboud University Nijmegen, PO Box 9010, 6500 GL Nijmegen, The Netherlands
- ²⁶⁰ Department of Physics, University of Notre Dame, Notre Dame, IN 46556, USA
- ²⁶¹ Consiglio Nazionale delle Ricerche – Istituto dei Sistemi Complessi, Piazzale Aldo Moro 5, 00185 Roma, Italy
- ²⁶² Korea Astronomy and Space Science Institute (KASI), Yuseong-gu, Daejeon 34055, Korea
- ²⁶³ Hobart and William Smith Colleges, Geneva, NY 14456, USA
- ²⁶⁴ International Institute of Physics, Universidade Federal do Rio Grande do Norte, Natal, RN 59078-970, Brazil
- ²⁶⁵ Museo Storico della Fisica e Centro Studi e Ricerche “Enrico Fermi”, 00184 Roma, Italy
- ²⁶⁶ Lancaster University, Lancaster LA1 4YW, UK
- ²⁶⁷ Università di Trento, Dipartimento di Matematica, 38123 Povo, Trento, Italy
- ²⁶⁸ Indian Institute of Science Education and Research, Pune, Maharashtra 411008, India
- ²⁶⁹ Dipartimento di Fisica, Università degli Studi di Torino, 10125 Torino, Italy
- ²⁷⁰ Indian Institute of Technology, Palaj, Gandhinagar, Gujarat 382355, India
- ²⁷¹ Department of Physics, Kyoto University, Sakyou-ku, Kyoto, Kyoto 606-8502, Japan
- ²⁷² Department of Electronic Control Engineering, National Institute of Technology, Nagaoka College, Nagaoka, Niigata 940-8532, Japan
- ²⁷³ Departamento de Matemática da Universidade de Aveiro and Centre for Research and Development in Mathematics and Applications, Campus de Santiago, 3810-183 Aveiro, Portugal
- ²⁷⁴ Marquette University, 11420 W. Clybourn St., Milwaukee, WI 53233, USA
- ²⁷⁵ Graduate School of Science and Engineering, Hosei University, Koganei, Tokyo 184-8584, Japan
- ²⁷⁶ Faculty of Science, Toho University, Funabashi, Chiba 274-8510, Japan
- ²⁷⁷ Faculty of Information Science and Technology, Osaka Institute of Technology, Hirakata, Osaka 573-0196, Japan
- ²⁷⁸ Università di Firenze, Sesto Fiorentino 50019, Italy
- ²⁷⁹ INAF, Osservatorio Astrofisico di Arcetri, Largo E. Fermi 5, 50125 Firenze, Italy
- ²⁸⁰ Indian Institute of Technology Hyderabad, Sangareddy, Khamdi, Telangana 502285, India
- ²⁸¹ iTHEMS (Interdisciplinary Theoretical and Mathematical Sciences Program), The Institute of Physical and Chemical Research (RIKEN), Wako, Saitama 351-0198, Japan
- ²⁸² INAF, Osservatorio di Astrofisica e Scienza dello Spazio, 40129 Bologna, Italy
- ²⁸³ Department of Space and Astronautical Science, The Graduate University for Advanced Studies (SOKENDAI), Sagamihara, Kanagawa 252-5210, Japan
- ²⁸⁴ Andrews University, Berrien Springs, MI 49104, USA
- ²⁸⁵ Research Center for Space Science, Advanced Research Laboratories, Tokyo City University, Setagaya, Tokyo 158-0082, Japan
- ²⁸⁶ Institute for Cosmic Ray Research (ICRR), Research Center for Cosmic Neutrinos (RCCN), The University of Tokyo, Kashiwa, Chiba 277-8582, Japan
- ²⁸⁷ National Metrology Institute of Japan, National Institute of Advanced Industrial Science and Technology, Tsukuba, Ibaraki 305-8568, Japan

- ²⁸⁸ Dipartimento di Scienze Aziendali – Management and Innovation Systems (DISA-MIS), Università di Salerno, 84084 Fisciano, Salerno, Italy
- ²⁸⁹ Van Swinderen Institute for Particle Physics and Gravity, University of Groningen, Nijenborgh 4, 9747 AG Groningen, The Netherlands
- ²⁹⁰ Faculty of Science, Department of Physics, The Chinese University of Hong Kong, Shatin, NT, Hong Kong
- ²⁹¹ Vrije Universiteit Brussel, Boulevard de la Plaine 2, 1050 Ixelles, Belgium
- ²⁹² Department of Communications Engineering, National Defense Academy of Japan, Yokosuka, Kanagawa 239-8686, Japan
- ²⁹³ Department of Physics, University of Florida, Gainesville, FL 32611, USA
- ²⁹⁴ Department of Information and Management Systems Engineering, Nagaoka University of Technology, Nagaoka, Niigata 940-2188, Japan
- ²⁹⁵ Vrije Universiteit Amsterdam, 1081 HV Amsterdam, The Netherlands
- ²⁹⁶ Department of Physics and Astronomy, Sejong University, Gwangjin-gu, Seoul 143-747, Korea
- ²⁹⁷ Department of Electrophysics, National Chiao Tung University, Hsinchu, Taiwan
- ²⁹⁸ Department of Physics, Rikkyo University, Toshima-ku, Tokyo 171-8501, Japan

Appendix A: Other marginal candidate events

Table A.1. Other marginal candidate event list. We find three candidate events that passed a FAR threshold of 0.5 yr^{-1} in at least one of the three dedicated searches and additionally have a combined p-value less than 0.7.

Event	GPS Time (s)	cWB FAR (yr^{-1})	PyCBC FAR (yr^{-1})	GstLAL FAR (yr^{-1})	\bar{p}
190924_232654	1253402832.9	-	$9.0 \times 10^{+1}$	4.0×10^{-1}	6.5×10^{-1}
191225_215715	1261346253.8	-	4.7×10^{-1}	$2.0 \times 10^{+3}$	6.5×10^{-1}
191223_014159	1261100537.6	-	-	4.6×10^{-1}	7.0×10^{-1}

Table A.1 summarizes the other marginal candidates identified by our combined IMBH search in O3 data that are not reported elsewhere in a catalog of compact binary coalescence events and that satisfy the criteria described in Sect. 3.4. These triggers were reported by at least one of the contributing searches with a FAR below 0.5 yr^{-1} and have a $\bar{p} \leq 0.7$.

The event 191225_215715 was first reported by PyCBC Live (Dal Canton et al. 2021), a low-latency matched-filter search with a FAR of 0.4 yr^{-1} . When the contributing searches conducted a dedicated offline analysis, the PyCBC-IMBH search identified it with a FAR of 0.47 yr^{-1} . However, the cWB and GstLAL-IMBH searches did not identify the event. The transient did not pass cWB veto threshold as discussed in Sect. 3.1. The event is, however, identified by the most general cWB search for GW bursts of short duration with a FAR of $\sim 2 \text{ yr}^{-1}$, which is still consistent with the noise origin. The model-agnostic BayesWave (BW) analysis (Cornish & Littenberg 2015; Cornish et al. 2021) also identified the event with a FAR of $\sim 1 \text{ yr}^{-1}$. The event morphologically resembles the Tomte class of glitches (Davis et al. 2021), which are common but of unknown origin. Follow-up of LIGO Livingston data also showed the existence of multiple comparable glitches within 100 s of the event time.

The remaining two events, 190924_232654 and 191223_014159, were likely caused by instrumental noise. In the case of 190924_232654, fast light scattering noise extending up to about 60 Hz is present in the LIGO Livingston data around the time of the event, and there is a high-S/N glitch in the Virgo data. The time-frequency morphology of the 191223_014159 signal in the LIGO Livingston data matches an instrumental glitch (Davis et al. 2021).

Appendix B: Follow-up studies of 200114_020818

The cWB offline search detects 200114_020818 with a combined FAR of 0.058 yr^{-1} . The network S/N with an LHO-LLO network is 12.3, and the three-detector-network S/N is 14.5. Although we cannot exclude the terrestrial origin of 200114_020818, we did perform several follow-up studies on this candidate, which we summarize here. The studies include event reconstruction by BayesWave (BW) and cWB, parameter estimation (PE) with models of black hole binary merger including effects of orbital precession and higher order multipole emission, reconstruction of PE sample waveforms and a comparison to the event reconstruction with cWB, and residual analysis with BW.

B.1. Investigation of instrumental noise

As mentioned in Sect. 4, an instrumental noise transient at the Hanford observatory coincides with 200114_020818. The noise originates from a fan on a laser controller located on top of

a squeezed light optics enclosure. At the time of the event, an accelerometer detected a second-long frequency dip in the 76 Hz fan motion. Such vibration transients can weakly couple to the strain data through the squeezing system. We performed a follow-up investigation using the methods described in Nguyen et al. (2021) to acquire accurate estimates of the vibration coupling between the table accelerometer and the strain channel. We estimate the expected noise in the strain channel at the fundamental frequency to be over an order of magnitude below background levels, so the fan is highly unlikely to account for the event candidate; however, the estimated noise at the first harmonic (152 Hz) is about a factor of two below the background and could potentially impact parameter estimation.

B.2. Event reconstruction by model-independent analysis

We reconstructed the signal using two model-independent analyses, namely cWB (used in the searches) and BW. The BW algorithm constructs the signal as a linear combination of sine-Gaussian wavelets and does not use any astrophysical model. The cWB reconstructs the multi-detector maximum likelihood signal by using the inverse wavelet transformation with selected pixels. In Fig. B.1, the red colored solid and dotted blue curves correspond to the whitened reconstructed signal from cWB and BW, respectively. The cWB event reconstruction is within the 90% credible region of the event reconstruction by BW (blue shaded region) for all three detectors. The BW S/N is 4, 14, and 5 in LHO, LLO, and Virgo, respectively, while cWB S/N is 5, 12, and 6, obtained from the reconstructed event.

B.3. PE analysis

Here, we investigate the possibility that 200114_020818 may be described by the merger of a quasi-circular BBH system. We thus carried out a parameter estimation with up-to-date waveform models including effects of precession and higher order multipole moments. Specifically, we used three quasi-circular BBH waveform models $h(t; \theta)$: i) the numerical relativity surrogate model NRSur7dq4 (Varma et al. 2019); ii) the effective one-body model SEOBNRv4PHM (Ossokine et al. 2020; Babak et al. 2017); and iii) the phenomenological model IMRPhenomXPHM (Pratten et al. 2021). We performed the analysis on 8 s of data centered around 200114_020818. All analyses were performed on C01 60 Hz subtracted data with a lower cutoff frequency of 10 Hz and reference frequency of 11 Hz. For the IMRPhenomXPHM analysis, we used the nested sampling algorithm as implemented in LALInference (Veitch et al. 2015), while for SEOBNRv4PHM and NRSur7dq4 analyses we use the RIFT (Lange et al. 2017) analysis tool instead. Both algorithms are designed to compute the joint 15-dimensional posterior distribution $p(\theta|D, H)$. The evidence computed via Eq. 5

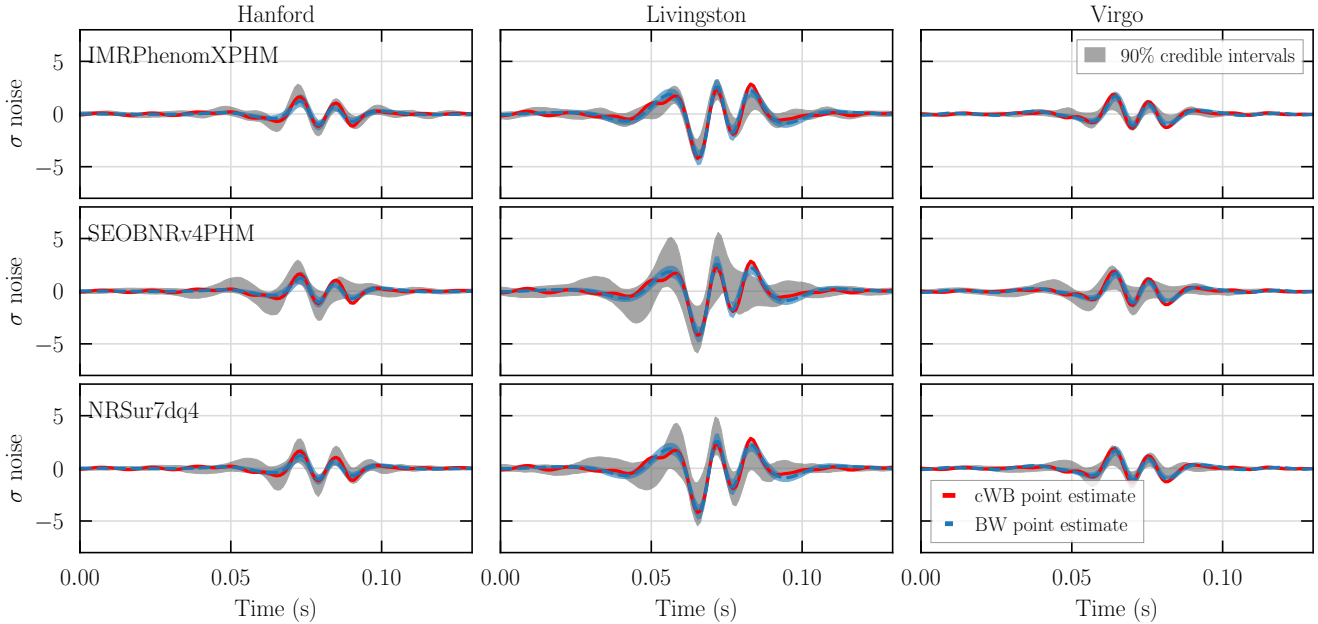


Fig. B.1. Consistency of the waveform reconstruction by cWB with three waveform models in the time domain: IMRPhenomXPHM (upper panel), SEOBNRv4PHM (middle panel), and NRSur7dq4 (lower panel). The colored solid red and dashed blue curves correspond to the whitened reconstructed event by cWB and Bayeswave, respectively. The blue shaded region corresponds to the 90% credible region from the event construction by BW. The gray shaded belts are reconstructed waveforms by cWB for the 90% credible interval corresponding to the PE runs.

Table B.1. Summary of median and 90% credible intervals of 200114_020818 for different waveform models. The columns show the waveform model used for parameter estimation, the source frame component masses m_i , effective spin parameters χ_{eff} and χ_p , luminosity distance D_L , the angle between the total angular momentum and the direction of propagation of the gravitational wave signal θ_{JN} , and the \log_{10} Bayes Factor between the signal and Gaussian noise given the model.

Waveform Model	m_1 (M_\odot)	m_2 (M_\odot)	χ_{eff}	χ_p	D_L (Mpc)	θ_{JN}	$\log_{10} B_{\text{SN}}$
IMRPhenomXPHM	$197.2^{+22.6}_{-31.2}$	$62.1^{+11.1}_{-16.6}$	$-0.3^{+0.1}_{-0.2}$	$0.6^{+0.1}_{-0.2}$	$593.4^{+276.8}_{-146.7}$	$0.9^{+0.8}_{-0.3}$	24.9
SEOBNRv4PHM	$179.6^{+17.1}_{-60.4}$	$26.7^{+7.3}_{-6.4}$	$-0.7^{+0.2}_{-0.1}$	$0.2^{+0.3}_{-0.2}$	$475.6^{+199.1}_{-153.0}$	$1.6^{+1.2}_{-1.1}$	26.2
NRSur7dq4	$75.0^{+32.9}_{-18.8}$	$42.5^{+16.4}_{-18.0}$	$-0.5^{+0.3}_{-0.2}$	$0.5^{+0.3}_{-0.3}$	$1797.0^{+1601.0}_{-1027.0}$	$2.0^{+0.9}_{-1.6}$	22.3

may be employed for model selection; the evidence for the signal hypothesis H, described by a specific model with given priors, is compared to the evidence for the null hypothesis N, according to which no signal is present, by computing the (\log_{10}) Bayes factor as given by

$$\log_{10} B_{\text{SN}} = \log_{10} \frac{p(d|H)}{p(d|N)}. \quad (\text{B.1})$$

The $\log_{10} B_{\text{SN}}$ ³ is tabulated in Table B.1 for all the three runs. The values of $\log_{10} B_{\text{SN}}$ indicate a preference for the hypothesis H that a signal is present over the alternative of only Gaussian noise.

These results do not, however, address the possibility that excess power in one or more detectors may be due to an instrumental artifact (glitch). As a diagnostic, we therefore performed a coherence test (Veitch & Vecchio 2008) using the IMRPhenomXPHM waveform model. The coherence test computes the Bayes factor for the coherent signal hypothesis against the hypothesis of an incoherent signal in the network of detectors. It can be thus interpreted loosely as an indicator of the presence of accidentally coincident noise artefacts that could mimic an astrophysical signal. The resulting \log_{10} Bayes factor for coherent versus incoherent signal 0.2, providing little to no evidence

in support of the coherent signal hypothesis. Such insignificant evidence is easily understood by looking at the \log_{10} Bayes factors computed from analyses of each individual detector's data: both Hanford-only and Virgo-only analyses recover a \log_{10} Bayes factor for the signal versus Gaussian noise hypothesis of 0.2. As a consequence, the posterior distributions from the Hanford- and Virgo-only analyses are largely uninformative. On the other hand, a Livingston-only analysis finds a \log_{10} Bayes factor of 25. Hence, from the parameter estimation point of view, 200114_020818 is essentially a single detector event. Returning to the results under the hypothesis H of a quasi-circular merger signal plus Gaussian noise, we summarize the resulting median and symmetric 90% credible regions for a few astrophysically relevant parameters from each of the models in Table B.1.

Figure B.2 shows the joint posterior distribution for the component masses m_1 and m_2 of the source according to each waveform model. The three models infer BH masses that are largely inconsistent. In particular, the inferred values – median and 90% credible intervals – show little overlap (see Table B.1). Moreover, the result from SEOBNRv4PHM shows a hint of bimodality in the mass posterior distributions.

The posterior distributions for the spin parameters (Fig. B.2) tell a similar story. If we compare the joint posterior distributions for the effective spin parameter χ_{eff} along the direction of the orbital angular momentum and the in-plane effective

³ The uncertainties on the individual $\log_{10} B_{\text{SN}}$ are ~ 1 .

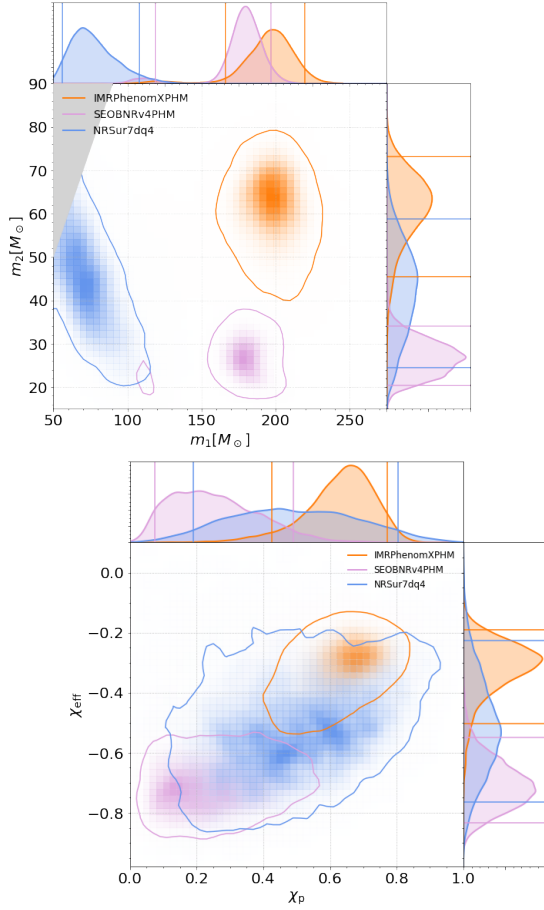


Fig. B.2. Posterior distributions: (left) Source mass distribution and (right) the effective spin and effective in-plane spin distribution of 200114_020818 for different waveform models. The 90% credible regions are indicated by the solid contour in the joint distribution and by solid vertical and horizontal lines in the marginalized distributions.

spin parameter χ_p , we find that the IMRPhenomXPHM and SEOBNRv4PHM probability distributions are disjointed at the 90% credible level. NRSur7dq4 instead recovers a posterior distribution that is much broader and encompasses both the posterior from IMRPhenomXPHM and SEOBNRv4PHM. With reference to Table B.1, all the three results indicate a preference toward the system being precessing and their spin vectors anti-aligned compared to the orbital angular momentum. Spin vectors anti-aligned with the orbital angular momentum have the effect of accelerating the dynamical evolution of the system toward coalescence, resulting in shorter GW signals for a given chirp mass.

In summary, a follow-up investigation of the properties of 200114_020818 interpreted as a possible quasi-circular binary merger shows considerable inconsistencies between results obtained by different waveform models. This is exemplified by the different posterior distributions for the BH masses as well as for their spins. Together with the lack of coherence among different detectors, our analysis indicates that, while we cannot exclude that 200114_020818 has an astrophysical origin, there is no consistent support for its interpretation as a quasi-circular binary merger.

B.4. Residual analysis

We evaluated the consistency of parameter estimation using the IMRPhenomXPHM waveform via two further analyses with

BW. We obtain a match between the BW event reconstruction waveform with the maximum-likelihood waveform from the IMRPhenomXPHM PE study as 0.871, which is consistent with expectations (Ghonge et al. 2020). Furthermore, we performed a signal residual test by subtracting the maximum likelihood IMRPhenomXPHM waveform from the data and analyzed the resulting residual with BW: the S/N obtained from the subtracted data is 7.4 for the LLO-LHO-Virgo network. In parallel, we estimated the distribution of S/N expected in noise from different time segments of O3 data. We estimated a p-value of 0.31 by comparing the distribution of noise S/N with the actual event residual value. This study does not show significant evidence for excess noise.

B.5. Comparison between event reconstruction and injection recovery with PE samples

Here, we compare the cWB reconstructed waveforms of the event with the waveforms estimated by the PE analysis (Szczepański et al. 2021; Gayathri et al. 2022; Salemi et al. 2019). We injected the waveforms corresponding to the PE samples into O3 data, estimated the reconstructed waveform for each of these samples using cWB, and compared it with the reconstructed event by cWB. In Figure B.1, the gray shaded belts are 90% confidence intervals obtained with the cWB reconstruction of PE samples for each waveform. We observe that the cWB (solid red) and BW event (dashed blue) reconstructions are largely within this gray shaded belt. Furthermore, we note that the time-domain reconstruction with the SEOBNRv4PHM and NRSur7dq4 samples have broader error belts compared to the reconstruction with the IMRPhenomXPHM samples. This is possibly due to broad posteriors and errors in cWB reconstruction.

To quantify the consistency between the cWB reconstruction and PE waveforms, we first computed the *null distribution* as the overlap between a injected waveform from the posterior distribution and its reconstructed waveform from the cWB. The source distribution is the distribution of the overlap between injected waveform from the posterior sample and the cWB event reconstruction of 200114_020818. The spread in the null distribution owes to the cWB reconstruction, noise fluctuation, and the posterior distribution. The spread in source distribution shows disagreement between the cWB event reconstruction and injected waveform from the posterior distribution. If the PE samples accurately describe any event, we expect a significant intersection between these two distributions. The p value of the null distribution is the fraction of samples in the distribution below the overlap between the maximum likelihood waveform and the reconstructed event. The p values for 200114_020818 are 0.01%, 0.4%, and 48%, corresponding to the SEOBNRv4PHM, NRSur7dq4, and IMRPhenomXPHM posterior samples, with source overlaps for the maximum-likelihood waveforms of 0.5, 0.68, and 0.86, respectively. Thus, the low overlaps and p values for the SEOBNRv4PHM and NRSur7dq4 waveform models indicate that these models are inconsistent with the cWB reconstruction.

In a separate study, we injected IMRPhenomXPHM PE samples and recovered the simulated events with cWB using the LHO-LLO and three-detector networks. We observe a 25% and 34% injection recovery in the LHO-LLO and LHO-LLO-Virgo configurations, respectively. The three-detector network recovers more events compared to the LHO-LLO network since LHO-LLO has blind and null spots in the sky. If the LHO-LLO-Virgo network saw the same population of signals as the LHO-LLO network, then we would not reanalyze the data with the LHO-LLO-Virgo network. 73% of the recovered injections

by the three-detector configuration is not recovered by LHO-LLO. However, out of the 34% of samples recovered by the LHO-LLO-Virgo analysis, only 8.65% of these samples have the same or higher significance than the 200114_020818 event. When we look at the detector network sensitivity skymaps, we find that it is not surprising that this event is missed by the LHO-LLO network. We conclude that the significance estimated for 200114_020818 is unlikely to result from a quasi-circular BBH with binary parameters according to `IMRPhenomXPHM`.

The detailed analyses of 200114_020818 under the quasi-circular BBH merger hypothesis give inconsistent results across

different waveform approximants with precession and higher order multipole moments. This along with the residual study indicates that there is no consistent interpretation of the signal with the available quasi-circular merger waveforms. However, the unmodeled event reconstructions are consistent with each other. Hence, either the event is not consistent with the available quasi-circular binary black hole waveforms, or its origin is non-astrophysical in nature. We do not report any alternative scenario such as an eccentric binary merger due to lack of availability of waveforms that include both eccentricity and orbital precession.